Simultaneous profiling of spatial gene expression and chromatin accessibility for mouse brain development

Fuqing Jiang[1,#], Xin Zhou[1,#], Yingying Qian[2,3,#], Miao Zhu[2,#], Li Wang[2], Zhuxia Li[2], Qingmei Shen[1], Fangfang Qu[1], Guizhong Cui[1], Kai Chen[4], Guangdun Peng[1,2,5,*]

[1]Center for Cell Lineage and Atlas, Bioland Laboratory, Guangzhou 510005, China
[2]Center for Cell Lineage and Development, CAS Key Laboratory of Regenerative Biology, Guangdong Provincial Key Laboratory of Stem Cell and Regenerative Medicine, GIBH-HKU Guangdong-Hong Kong Stem Cell and Regenerative Medicine Research Centre, University of Chinese Academy of Sciences, Guangzhou Institutes of Biomedicine and Health, Chinese Academy of Sciences, Guangzhou 510530, China
[3]University of Science and Technology of China, Hefei 230026, China
[4]Yunnan Key Laboratory of Primate Biomedical Research, Institute of Primate Translational Medicine, Kunming University of Science and Technology, Kunming, 650500, China
[5]Institute for Stem Cell and Regeneration, Chinese Academy of Sciences, Beijing 100101, China
#: equal contribution
*: corresponding author, email: peng_guangdun@gibh.ac.cn

Brain are complex biological tissues which function relies on coordinated anatomical and molecular structure comprised by a large number of specialized cells. The spatial architecture of brain which is key to the understanding of its physiological and pathological significance is formed during embryo development. However, the molecular basis for discrete neuroanatomical domains particularly in the context of spatial organization of the brain is inadequate. Here, we introduced microfluidic indexing based spatial ATAC and RNA sequencing (MISAR-seq), a method for joint profiling of chromatin accessibility and gene expression with spatial information retained in the developing mouse brain. Our study has established a direct means to spatially determine the coordination between chromatin accessibility and transcriptome, identified the chromatin potential to define cell fate determination of brain organization, and uncovered spatio-temporal regulatory principles during mammalian brain development.

The brain is an enormously complex organ that composed of spatially organized and functionally interconnected neurons, glia and non-neural cells. An entry point in understanding brain

development and function is to annotate the atlas of the brain by highly scalable and unbiased single-cell multi-omics approaches[1-4]. In recent years, brain region formation and cell maturation process have been profiled using a variety of single cell technologies, including single cell RNA sequencing (scRNA-seq)[2], single nuclear ATAC sequencing (snATAC-seq)[5, 6], single cell multimodal technologies[7] and single cell joint multi-omics sequencing[3], which uncovered the complex interplay of brain neurons cell-cell interaction and led to the deep understanding of intrinsic genetic programs of multiple cell types. With the advent of spatial transcriptome technologies[8, 9], the molecular cytoarchitecture of the brain has been unveiled in unprecedented detail. A complete description on spatially resolved transcriptome atlas for the developing and adult brain is on the horizon. However, one big challenge to define the building blocks of brain function lies in deciphering the complex regulatory network, e.g. the connection between chromatin modification and its transcription output, in forming the sophisticated tissue organization.

Similar to the advances in single-cell sequencing, spatial multiomics is the new frontier for linking measurements from layers of genome, epigenome, transcriptome and proteomes at the spatial level to reveal regulatory and functional mechanisms. In the past few years, there has been a rapid emergence of spatial transcriptome technologies on different platforms, together with the infant spatial epigenome, greatly expanding the toolkits for our understanding the interplay of biological networks. Importantly, different modalities of spatial dimension (e.g., spatial-ATAC-seq[10], spatial-cut&tag[11]) can be achieved individually, there is a requisite to simultaneously profile the gene expression and regulatory genomic information in the spatial context on a large scale, by which insightful gene regulatory interactions can be gained and is essential for dissecting the basis of anatomical tissue architecture. Here, we reported a spatially resolved joint profiling of chromatin accessibility and gene expressions approach (MISAR-seq) and we applied it to mouse brain of consecutive developmental stages. We showed that high quality transcriptome-open chromatin status in the different anatomical brain regions can be delineated and our data revealed the dynamic spatiotemporal regulatory mechanisms in establishing the complex architecture of mouse brain.

Results

Overview of MISAR-seq design and data quality.

We devised a microfluidic indexing based spatial ATAC and RNA sequencing (MISAR-seq) method, motivated by DBiT-seq design[12] and SHARE-seq methodology[13] (Extended Data Fig. 1a-c). MISAR-seq includes the following steps (Extended Data Fig. 1a). First, we modified the flow of microchannels and sealing slabs to facilitate a leakage-prevent and minimized diffusion effect (Extended Data Fig. 1b,c). After fixed by 1% formaldehyde, Tn5 transposase assembled with read1 and read2 adaptor sequence is administrated to the tissue slide to label the open

chromatin regions in situ. The tissue slide is refixed and mRNA is reverse transcribed using a poly (T) primer bearing an 10bp unique molecular identifier (UMI), read2 anchor sequence and a biotin tag. Next, the tissue section is put onto the microfluidic chip and a set of DNA barcode round1_i (i = 1 to 50) are flowed over the tissue surface through microchannel-guided delivery to ligate to the read2 anchors. A second set of DNA barcode round2_i are flowed over the same tissue surface through microchannels perpendicular to the tissue slides and are attached to the ends of the barcode 1. These two rounds of ligation ensure a spatial barcoding to paired ATAC and mRNA molecules of at most 2500 grids (currently 50 μm in width, representing around 15-30 cells). Adjacent sections are stained to obtain a high-sensitivity anatomical image for downstream alignment. As a validation of leakage-free, Cy3 and Fam dyes are added with the two rounds of barcodes respectively. Additionally, these two dyes can form a 2D mosaic pattern on the tissue slides for coordinates calibration aided with hematoxylin and eosin (H&E) images (Extended Data Fig. 1d). Typically, we would get nucleosomal distribution library for ATAC, no less than 800 bp amplicons and 300~700 bp cDNA fragments for RNA library at the end of the experimental (Extended Data Fig. 1e-g).

We performed MISAR-seq on the fetal brain of E11.0, E13.5, E15.5 and E18.5 mouse embryo (Fig. 1a,b). For spatial ATAC of MISAR-seq, the TSS enrichment score calculated among the unique nuclear fragments showed higher coverage of TSSs, compared to 10x scATAC-seq data (Fig 1c) . A median of 16,472 to 34,730 unique fragments per grid was achieved after filtering low quality reads, of which between 15.0% to 45.6% fragments fell within peak regions (FRiP), indicating a high coverage and low background. In comparison, the unique fragments per cell from 10x scATAC-seq of E18.0 brain was 17,368 and the FRiP was 24.7%. A recently reported spatial-ATAC-seq based on similar platform had, on average, 36,303 unique fragments for E11.0 embryo and 100786 for E13.0 embryo while the FRIP value was 10.0% for E11.0 embryo and 8.0% for E13.0 embryo per gird in the same spatial resolution[11] (Fig. 1c and Extended Data Fig. 2a). The TSSs enrichment score calculated among the unique fragments showed higher coverage of TSSs, compared to 10x scATAC-seq and recent spatial-ATAC-seq data (Extended Data Fig. 2a). The fractions of read-pairs mapped to mitochondrial of each sample section were between 2.52% to 2.95%, which were slightly higher than 10x scATAC-seq platform but is reasonable due to the openness of the cells on tissue sections (Extended Data Fig. 2a). Meanwhile, our MISAR-seq showed typical nucleosomal and subnucleosomal fragments distribution (Extended Data Fig. 1e, 2b) and captured more transcription start sites (TSSs) compared to 10x scATAC-seq (Fig. 1c and Extended Data Fig. 2c and 3).

To further validate the ATAC data of MISAR-seq, we compared the MISAR-seq ATAC signals with bulk ATAC data from ENCODE at the same E15.5 brain tissue[14]. The results

showed that they shared major ATAC peaks in all forebrain, midbrain and hindbrain regions (Extended Data Fig. 4a-c). We also calculated the overlapped peaks from aggregated brain regions and found most of the peaks in the MISAR-seq ATAC study were also found in the Encode bulk data (Extended Data Fig. 4d-f).

Next, we evaluated the MISAR-seq RNA performance during the co-measurement of both modalities. Generally, the total number of UMIs and genes per gird were comparable or slightly better than DBiT-seq in the same 50 μm resolution[12] (Fig. 1d). The fractions of read-pairs mapped to mitochondrial and ribosome protein of each sample section were lower than those from DBiT-seq (Extended Data Fig. 5a). The tissue permeabilization and fixation is the key bottleneck to ensure the technical compatibility of both modalities. Interestingly, we introduced additional refixation by 4% formaldehyde before mRNA reverse transcription and found this treatment increased the yield and quality of the spatial transcriptome data (Extended Data Fig. 5b and Methods).

To explore the consistence of the MISAR-seq data on both modalities, the correlation analysis was performed between biological replicates of serial tissue sections for MISAR-seq ATAC data and we found very high data reproducibility (Fig. 1e). Moreover, we also aggregated the chromatin accessibility and mRNA reads from the same E15.5 forebrain (S1) section. Unsurprisingly, the results showed that the RNA reads were located in the 3' end and the peaks of DNA accessibility were located in the TSS region of the same gene, indicating we could deduce the chromatin-gene expression relationships in cells of the same spatial locations. Besides, the aggregated chromatin profiles from randomly selected 300 spatial grids of an E15.5 forebrain also faithfully reproduced the bulk measurement of chromatin accessibility obtained from the ENCODE data but had better signal-to-noise ratio, suggesting our MISAR-seq approach is robust (Fig. 1f).

The MISAR-seq data was also used to interrogate published scRNA-seq data from the same stage[2]. Take E15.5 brain (S1) as an example, we first performed single cell deconvolution by RCTD to examine the cell type distribution in each spatial grid (see Methods). We found the major cell type distributions have a good agreement with their spatial anatomical annotation (Fig. 1g). We then integrated both MISAR-seq data and scRNA-seq reference data and performed unsupervised clustering (see Methods). 11 clusters were obtained for MISAR-seq ATAC and 14 clusters for MISAR-seq RNA. Expectedly, we found that the cell types agree very well with the brain anatomical region. Then, the clusters were mapped to the spatial section and annotated by spatial anatomic or pseudo-tissue of the reference data separately (Fig. 1h-m). We found that the cell types agree very well with the brain anatomical regions. For example, forebrain dorsal in reference single-cell dataset were mapped to regions of the forebrain dorsal pallium intermediate, ventricular and superficial (Fig. 1j,m).

145

146 **Profiling of chromatin accessibility and gene expression in development embryo mouse**
147 **brain with MISAR-seq.**

148 Having the co-assay of spatial ATAC and RNA at E11.0, E13.5, E15.5 and E18.5 stages, we
149 sought to examine the comprehensive view of both parameters along the brain developmental
150 process. After filtering out non-tissue grids, a total of 7118 grids with both chromatin accessi-
151 bility and gene expression were obtained. To accommodate the integrative analysis of both
152 chromatin accessibility and transcriptome, we aligned cross-data in parallel using slices of
153 MISAR-seq ATAC. First, for ATAC profiles, a pixel by tile matrix was generated by aggregating
154 reads in 5 kilobase bins across the mouse genome and an ATAC ArchR object was created.
155 For RNA profiles, we use addGeneExpressionMatrix function to add RNA profiles in the ArchR
156 object. Then, latent semantic indexing (LSI) was applied for dimensionality reduction and Har-
157 mony was used to remove technical batch effects (see Methods). Setting a basic layer of com-
158 parison, a manual anatomical annotation was performed to reveal major tissue organization
159 following Kaufman's Atlas of Mouse Development and Allen Brain Atlas (Fig. 2h). We found
160 both spatial-ATAC clusters and spatial-RNA-seq clusters can faithfully recapitulate the tissue
161 organization in the developing mouse brain, with slightly different in minor details (Fig. 2). For
162 example, among the 11 ATAC or RNA clusters, ATAC cluster 2 or RNA cluster 4 represents
163 cartilage in the mouse embryo. ATAC cluster 5 and RNA cluster 5 are associated with forebrain
164 of dorsal pallium (DPallm), including the ventricular and mantle region of dorsal pallium. At
165 E11.0, the RNA profile showed higher resolution in defining the spatial structures compared to
166 ATAC information. Overall, the spatial ATAC and RNA clusters correlated well, which was
167 further demonstrated in the joint spatial clustering with integrated datasets. The combined
168 clusters also showed that the spatial complexity was increased gradually along the brain de-
169 velopment, with more discrete cell clusters emerged at E18.5 (Fig. 2e-g). Besides, the analysis
170 from replicate sections obtained similar results (Extended Data Fig. 6). Together, our data
171 shows that major anatomical structures can be readily delineated by spatially resolved chro-
172 matin and transcriptome profiling.

173

174 **Integrated analysis of chromatin accessibility and gene expression across brain tissue**
175 **types.**

176 To fully reveal the relationship and molecular mechanisms between chromatin state and gene
177 expression, the chromatin- and transcriptome-based spatial cell clustering were compared.
178 We first evaluated the consistency between the cell clusters based on independent modality
179 and found a high fraction of cells were shared by respective ATAC and RNA clusters (Fig. 3a).

By connecting the ATAC clusters with RNA clusters, we found that the overall patterns of chromatin accessibility were associated with more diverse gene expression clusters (Fig. 3a,b), indicating a lower clustering power for ATAC information possibly owing to the sparsity of chromatin data that are still undergoing maturation. For example, two ATAC clusters 2 and 9 which are mostly present at E11.0 were evolved into many RNA clusters at late stages. We also found that the grid composition of the clusters became more distinct during brain development, indicating an increased consolidation of tissue identity (Fig. 3c).

Next, we aimed to find the signature features related to each cluster. With ArchR, we are able to generate "gene activity score" to enable accurate cluster annotation (see Methods). In summary, we identified 571 marker genes in ATAC-based clusters and 2473 marker genes in RNA-based clusters across the integrated 14 tissue types, in which, many of these markers showed cluster-specific expression and can be validated by in situ hybridization data from Allen Mouse Brain Atlas (Fig. 3d,e and Extended Data Fig. 7). We selected the top15 marker genes to perform Gene Ontology (GO) analysis, and found the annotations were consistent between two modalities and aligned well with their anatomical structures. Furthermore, as reported in other dual-omics assay, the cell-type identities of the major clusters were better supported by specific accessible chromatin accessibility in promoter regions of marker genes (Fig. 3f)[15].

MISAR-seq identified regulatory machinery for mouse brain development

To disentangle the complexity of gene regulatory networks that drive brain development, we sought to identify the regulatory mechanisms that function for establishing the spatial organization of the mouse brain. To this end, we first created pseudo-bulk replicates based on the combined clusters using the addReproduciblePeakSet function of ArchR and called peaks with MACS2 considering per-cell ATAC-seq data is essentially binary (accessible or not accessible) (see Methods). We counted the number of peaks and found that there are high proportion of promoter and distal peaks in each cluster, indicating that a lot of regulatory elements were obtained in our MISAR-seq ATAC data (Extended Data Fig. 8a). We identified a total of 30272 signature peaks enriched in each cluster and labeled the top 4 peaks in the heatmap, in which, most clusters had high numbers of differential peaks (Extended Data Fig. 8b).

Next, we performed motif enrichment analysis based on differential peaks of each cluster with motif database CISBP(v2) using the function of peakAnnoEnrichment from ArchR (see Methods). We obtained 37 enriched motifs in total and found the corresponded transcription factors (TF) showed a tissue-specific distribution (Fig. 4a). For example, motifs of *Myod1*, *Myog* and *Myf5* were enriched in cluster 1 where represents the muscle cells[16]. Motifs of *Neurod1*, *Neurod4* and *Neurod6* were highly enriched in cluster 8 of DPallm, corroborating their

216 reported role in regulating neuronal progenitor differentiation and neuronal specification in the
217 cerebral cortex[17]. Interestingly, the cluster 8 also possess the highest abundance of peaks and
218 motifs, suggesting a predominant presence in mice brain development (Fig. 4a and Extended
219 Data Fig. 8b).

220 To further predict the TF enrichment on a per-grid basis from the sparse chromatin acces-
221 sibility data, we calculated the variability deviation for the enriched motifs (see Methods). In-
222 terestingly, after ranked the TFs by variable deviation, we found the top 21 TFs could be
223 roughly classified into a few major TF families, including *Rfx* family, *Runx* family and basic
224 Helix-loop-Helix (bHLH) family. The bHLH family members such as *Ascl1*, *Ascl2*, *Neurod1*,
225 *Neurod4*, *Neurod6* and *Atoh1* were well- known master regulators of cell proliferation and neu-
226 ronal specification[16]. *Rfx* TFs were reported to have both redundant and specific functions in
227 ependymal cell of the brain ventricle[18]. To further uncover the detailed regulatory mechanisms
228 under mouse brain development, we performed peak-gene lineage analysis and identified
229 11772 peak-gene linkages by ArchR and these linkages were divided into 15 modules accord-
230 ing to the pattern of chromatin accessibility and gene expression (Fig. 4c and Methods). Not
231 surprisingly, the chromatin accessibility modules and transcriptome modules have a good con-
232 sistence with each other. To reveal the potential regulatory function of those peak-gene link-
233 ages in brain, the top ranked TFs of *Neurod1* and *Rfx2* were selected to represent the regula-
234 tion in cortex region or in the diencephalon and hindbrain region, respectively (Fig. 4a,b). The
235 TF footprinting analysis of *Neurod1* and *Rfx2* predicted their enriched binding locations for the
236 corresponding brain regions (Fig. 4d and Extended Data Fig.10b). The region-specific pro-
237 moter activity of these TFs can be verified in the chromatin accessibility, gene expression, TF
238 deviation score and in situ hybridization data from Allen Mouse Brain (Fig. 4e-g and Extended
239 Data Fig. 10a). After scanning the motif of Neurod1 and Rfx2 in all peak-gene linkages, we
240 obtained 328 motif sites for *Neurod1* and 697 motif sites for *Rfx2*. We showed the significant
241 motif sites for *Neurod1* and *Rfx2* (peak-gene correlation >= 0.7, Fig. 4b,c). Unexpectedly, we
242 found *Neurod2*, *Dync1i1*, *Neurod6* and *Igfbpl1* were enriched in DPall regions for *Neurod1*
243 motif and *Igfbpl1*, *Dpysl5*, *Nyap1*, *Atp1a3* and *Pou2f2* were enriched in DPall, diencephalon
244 and hindbrain for *Rfx2* motif (Fig. 4c), indicating the TFs function have a high correlation with
245 their tissue location. The genome track plot showed that *Neurod1* motif was located at the
246 promoter or enhancer region of *Neurod2* and *Neurod6*, suggesting both of them can be directly
247 regulated by *Neurod1*[19]. Meanwhile, We also identified other dynamically regulated promoter
248 interactions with specific enhancers by peak gene linkages and peak co-accessibility analysis
249 (Fig. 4h,i and Extended Data Fig. 9e). Besides, the Neurod1-regulated target genes also
250 showed region-specific expression in DPall regions (Extended Data Fig. 7e,10d and 10e).
251 These are also reflected in the *Rfx2 motif and Rfx2*-regulated targets e.g. *Pou2f2*, *Nyap1*,

252 *Atp1a3* and *Dpysl5* (Extended Data Fig. 9a-d, Extended Data Fig. 11). Interestingly, we found
253 *Igfbl1*, the member of insulin-like growth factor binding proteins, can be regulated by both *Neu-*
254 *rod1* and *Rfx2* because both motifs were found in its promoter or enhancer region. The chro-
255 matin accessibility and gene expression of *Igfbpl1* proved the specific activation in DPall region
256 (Fig. 4j and Extended Data Fig. 10c), in line with the reported role of *Igfbpl1* as important
257 regulator in the development of mouse forebrain[20].
258 All together, we uncovered the signature TFs for each cluster based on the differential
259 peaks and identified key regulators that enrich in specific brain regions using peak-gene ex-
260 pression correlation revealed by the co-mapping of spatial ATAC and spatial RNA profile.
261
262 **Molecular dynamic and gene regulatory network of corticogenesis.**
263 Corticogenesis is a complex development process characterized by the proliferation, differen-
264 tiation, and migration of cortex progenitor cells, and the inside-out gradient of neurogenesis.
265 The regulatory mechanism of cis-regulatory elements such as enhancers and promoters are
266 central for cortical neuron cell fate determination and laminar structure organization. Empow-
267 ered by the unique ability of joint mapping the spatial ATAC and RNA data, we anticipated that
268 asynchronous cell fate determination and cascade regulation may be illustrated through the
269 integration of both modalities in a spatial and temporal manner.
270 We first selected the combined peak accessibility and gene expression that map to the
271 cortex regions from the united UMAP clusters to infer the corticogenesis trajectory (Fig. 5a, b,
272 see Methods). Of note, the pseudotime axis captured well the spatiotemporal changes in cor-
273 tex development (Fig. 5c, d and Methods). To connect the enhancer elements and gene ex-
274 pression, we applied a correlation-based method to the smooth pseudotime axis of the com-
275 bined manifold (see Methods). We identified 66,805 putative enhancer-to-gene linkages. In-
276 terestingly, highly enhancer-regulated genes (genes with a large number of peaks-gene link-
277 ages) (blue color in Fig. 5e) are associated with forebrain development and neuron differenti-
278 ation. For example, transcription factors such as *Sox2*, *Dlx2*, and *Hes* showed high expression
279 in early phase of the pseudotime (Fig. 5g). *Sox2* has a critical role in maintaining neuron stem
280 cells[21]. *Hes* genes are downstream targets of the *Notch* signaling pathway that represses pro-
281 neural genes and maintain neuron stem cells boundaries[22]. *Dlx* genes can function as modu-
282 lators to determine neuron versus oligodendrocyte cell fate[23]. Therefore, these results indicate
283 that the spatiotemporal trajectory analysis has the potential to identify important regulatory
284 mechanisms for early cortex cell fate determination.
285 To further analyze the dynamics of accessibility activity and gene expression along the
286 corticogenesis trajectory, we computed the domain of enhancer regulatory (DER) activity by
287 aggregating linked peak counts for each gene (see Methods). The generalized linear model

was fitted on each gene expression and accessibility activity score to select the pseudotime-dependent features. We identified 1160 dynamic regulatory interaction pairs and clustered them into 5 modules (Fig. 5g). Modules along the pseudotime were enriched in functions such as cell proliferation, neuron migration, axonogenesis, neuron projection, and synapse activity just in the developmental order of corticogenesis (Fig. 5h). Coordination of these interaction pairs indicates that a set of highly regulatory genes drive cell fate decision and determine lineages differentiation during corticogenesis. Of note, we observed a predominately asynchronous pattern between peak accessibility and gene expression at late pseudotime. For example, we noticed module 5 overall gained accessibility earlier than their gene expression apparently.

Next, we utilized FigR to infer the transcriptional regulators of target genes[24]. Integrated peak-to-gene links and motif enrichment in linked peak regions allow us to define many putative activators and repressors and construct the gene regulation network (Fig. 5i-l and Extended Data Fig. 12a). We found thyroid hormone receptor *Thra* is a node TF that connects many targets. Previously, thyroid hormone receptors have been suggested to play a crucial role in human and mouse cortical neurogenesis[25, 26]. However, the regulatory mechanism remains unknown. By integrating peak accessibility and gene expression, we found that motifs of *Neurod6* and *Mef2c* were enrichment in linked peaks of *Thra*, suggesting *Thra* may be positively regulated by *Neurod6* and *Mef2c* (Fig. 5i). Ordering along the pseudotime, *Neurod6* accessibility was increased first, followed by Thra accessibility, *Neurod6* RNA, and *Thra* RNA. Finally, *Mef2c* accessibility and RNA were increased toward the pseudotime endpoint (Fig. 5j). Interestingly, we also found that *Neurod6*, *Thra*, and *Mef2c* TFs show high centrality in the TF-targets network and are positively correlated with each other (Fig. 5k), pointing to a potential TF regulatory cascade during cortex development[27](Extended Data Fig. 12b). Hence, MISAR-seq has the power to map the gene regulatory logic of mouse corticogenesis and provides new insights for decoding the spatiotemporal dynamic of tissue organization.

Discussion

Recently, spatially resolved transcriptomics has been a technological frontier that reshapes biomedical research with emergence of many new methodologies and applications. Importantly, the architecture and tissue function are regulated across multiple layers, including epigenetic regulations such as modulation of gene expression by changes in histone modification and chromatin accessibility. Therefore, it is highly desirable to systematically examine the spatial gene expression together with epigenetic information directly in the same cell populations. In the current study, we reported a high-throughput method for simultaneous profiling

of chromatin accessibility and gene expression with spatial information retained. We demonstrated the utility of MISAR-seq by applying it to the mouse embryonic brain development at four developmental stages. Our results show that MISAR-seq can identify the chromatin potential and gene expression of the same spatial location. The integrative analysis enables us to define the cell fate determination of mouse fetal brain, and uncover the spatiotemporal regulatory principles during mammalian brain development.

It worth noting that currently the method has not achieved single-cell resolution, therefore making the defined interpretation of regulatory mechanisms or trajectory inference still challenging, considering pronounced heterogeneity exists in the spatial organization of diverse biological systems. Although we only presented data obtained on embryonic brain tissues, we have adapted the method to other tissue types such as tumor samples and achieved similar performance. Considering similar principle has been implemented in a recent spatial-ATAC-seq method and robust results can be obtained[10], we anticipate the MISAR-seq would be compatible for a wide range of tissue type. Future optimization to further increase the spatial resolution, the scalability and additional layers of omics information will provide versatile tools to disentangle the complexity of gene regulatory and cell–cell communication networks that drive cell functions and responses in structurally organized tissues.

References

1. Takei, Y. et al. Single-cell nuclear architecture across cell types in the mouse brain. *Science* **374**, 586-594 (2021).
2. La Manno, G. et al. Molecular architecture of the developing mouse brain. *Nature* **596**, 92-96 (2021).
3. Zhu, C. et al. Joint profiling of histone modifications and transcriptome in single cells from mouse brain. *Nat Methods* **18**, 283-292 (2021).
4. Rosenberg, A.B. et al. Single-cell profiling of the developing mouse brain and spinal cord with split-pool barcoding. *Science* **360**, 176-182 (2018).
5. Li, Y.E. et al. An atlas of gene regulatory elements in adult mouse cerebrum. *Nature* **598**, 129-136 (2021).
6. Preissl, S. et al. Deciphering the Epigenetic Code of Cardiac Myocyte Transcription. *Circ Res* **117**, 413-423 (2015).
7. Di Bella, D.J. et al. Molecular logic of cellular diversification in the mouse cerebral cortex. *Nature* **595**, 554-559 (2021).
8. Ortiz, C. et al. Molecular atlas of the adult mouse brain. *Sci Adv* **6**, eabb3446 (2020).
9. Ortiz, C., Carlen, M. & Meletis, K. Spatial Transcriptomics: Molecular Maps of the Mammalian Brain. *Annu Rev Neurosci* **44**, 547-562 (2021).
10. Deng, Y. et al. Spatial profiling of chromatin accessibility in mouse and human tissues. *Nature* (2022).

11. Deng, Y. et al. Spatial-CUT&Tag: Spatially resolved chromatin modification profiling at the cellular level. *Science* **375**, 681-686 (2022).
12. Liu, Y. et al. High-Spatial-Resolution Multi-Omics Sequencing via Deterministic Barcoding in Tissue. *Cell* **183**, 1665-1681 e1618 (2020).
13. Ma, S. et al. Chromatin Potential Identified by Shared Single-Cell Profiling of RNA and Chromatin. *Cell* **183**, 1103-1116 e1120 (2020).
14. Consortium, E.P. An integrated encyclopedia of DNA elements in the human genome. *Nature* **489**, 57-74 (2012).
15. Chen, S., Lake, B.B. & Zhang, K. High-throughput sequencing of the transcriptome and chromatin accessibility in the same cell. *Nat Biotechnol* **37**, 1452-1457 (2019).
16. Skinner, M.K., Rawls, A., Wilson-Rawls, J. & Roalson, E.H. Basic helix-loop-helix transcription factor gene family phylogenetics and nomenclature. *Differentiation* **80**, 1-8 (2010).
17. Tutukova, S., Tarabykin, V. & Hernandez-Miranda, L.R. The Role of Neurod Genes in Brain Development, Function, and Disease. *Front Mol Neurosci* **14**, 662774 (2021).
18. Lemeille, S. et al. Interplay of RFX transcription factors 1, 2 and 3 in motile ciliogenesis. *Nucleic Acids Res* **48**, 9019-9036 (2020).
19. Westerman, B.A., Chhatta, A., Poutsma, A., van Vegchel, T. & Oudejans, C.B. NEUROD1 acts in vitro as an upstream regulator of NEUROD2 in trophoblast cells. *Biochim Biophys Acta* **1676**, 96-103 (2004).
20. Gonda, Y. et al. Expression profiles of Insulin-like growth factor binding protein-like 1 in the developing mouse forebrain. *Gene Expr Patterns* **7**, 431-440 (2007).
21. Bani-Yaghoub, M. et al. Role of Sox2 in the development of the mouse neocortex. *Dev Biol* **295**, 52-66 (2006).
22. Kageyama, R., Ohtsuka, T. & Kobayashi, T. The Hes gene family: repressors and oscillators that orchestrate embryogenesis. *Development* **134**, 1243-1251 (2007).
23. Petryniak, M.A., Potter, G.B., Rowitch, D.H. & Rubenstein, J.L. Dlx1 and Dlx2 control neuronal versus oligodendroglial cell fate acquisition in the developing forebrain. *Neuron* **55**, 417-433 (2007).
24. Kartha, V.K. et al. Functional inference of gene regulation using single-cell multi-omics. *Cell Genomics*, 100166 (2022).
25. Krieger, T.G. et al. Mutations in thyroid hormone receptor alpha1 cause premature neurogenesis and progenitor cell depletion in human cortical development. *Proc Natl Acad Sci U S A* **116**, 22754-22763 (2019).
26. Bernal, J. Thyroid hormone receptors in brain development and function. *Nat Clin Pract Endocrinol Metab* **3**, 249-259 (2007).
27. Bradley, D.J., Towle, H.C. & Young, W.S., 3rd Spatial and temporal expression of alpha- and beta-thyroid hormone receptor mRNAs, including the beta 2-subtype, in the developing mammalian nervous system. *J Neurosci* **12**, 2288-2302 (1992).

Author contributions

G.P., and J.F. designed the study. J.F., X. Z., Y.Q., L.W. and S.Q. performed the experiments. J.F. and M.Z. analyzed the data with help from F.Q., G.C. and Z.L. K.C. provided reagents and suggestions. J.F. and G.P. wrote the manuscript with the help of others.

Acknowledgments

This work was supported in part by National Key R&D Program of China (2018YFA0107200, 2018YFA0801402), the "Strategic Priority Research Program" of the Chinese Academy of Sciences (XDA16020404), National Natural Science Foundation of China (31871456 and 32100483), Guangdong Basic and Applied Basic Research Foundation (2019B151502054, 2019A1515110985 and 2020A1515110517), Frontier Research Program of Bioland Laboratory (Guangzhou Regenerative Medicine and Health Guangdong Laboratory, 2018GZR110105013), Jiazi Research Innovative Project of Bioland Laboratory (2019GZR110108001), Science and Technology Planning Project of Guangdong Province (2020B1212060052). We thank Patrick Tam for discussions and critical reading of this study.

Figure information

Fig. 1 | Overview of MISAR-seq: data quality and validation. a, Overview of the sampled embryonic time points. **b**, H&E images from an adjacent tissue section. **c,** Comparison of TSS Enrichment value (top) and unique fragments (bottom) per grid between MISAR-seq and 10x scATAC-seq. Dashed lines indicate the results from Spatial-ATAC-seq[10.]. **d**, Comparison of UMIs (top) and genes number (bottom) per grid between MISAR-seq and DBiT-seq. **e**, Spearman correlation coefficient of bulk profiles from eight embryo mouse brain sections in this experiment. **f**, Aggregate selected forebrain spatial RNA and ATAC peak profile compared to published profiles of ATAC-seq in E15.5 mouse forebrain. **g**, Spatial distribution of E15.5 brain spatial RNA single cell deconvolution results with E15.5 brain scRNA-seq reference data. **h-j**, The clustering results of E15.5 mouse brain for spatial ATAC after integration with reference E15.5 brain scRNA-seq data. UMAP results annotated with reference (h) and anatomic (i) or spatial mapping (j). **k-m**, The clustering results of E15.5 mouse brain for spatial RNA after integration with reference E15.5 brain scRNA-seq data. UMAP results annotated with reference (k) and anatomic (l) or spatial mapping (m).

Fig. 2 | Spatial chromatin accessibility, gene expression and combined mapping for mouse brain development at E11.0, E13.5, E15.5 and E18.5. a-c, Spatial ATAC (a), RNA

438 (b) and combined (c) UMAP visualization of different mouse brain development stage, colored
439 by different clusters. **d**, Combined spatial ATAC and RNA UMAP visualization of integrated
440 different mouse brain development stage, colored by different sample sections. **e-g**, Unsuper-
441 vised clustering of mouse brain sections for spatial ATAC (e), RNA (f) and combined (g). **h**,
442 Anatomic annotation of major tissue regions based on the H&E images for different mouse
443 brain stages. DPallm, mantle zone of dorsal pallium. DPallv, ventricular zone of dorsal pallium.
444
445 **Fig. 3 | Combined analysis of chromatin accessibility and gene expression across de-**
446 **velopment stages of mouse brain. a**, Heatmap showing the proportion of cells in the ATAC
447 clusters that overlap with RNA clusters. **b**, Cluster connective changes between ATAC, RNA
448 and combined clusters shown in sankey plots. **c**, The proportion of cells in the combined clus-
449 ters for development stages of mouse brain. **d-e**, Heatmap of spatial ATAC (d) and RNA (e)
450 marker genes across all clusters. Select GO terms and top ranked genes are shown. **f**, Rep-
451 resentative genome browser views of marker genes from aggregated spatial ATAC data from
452 MISAR-seq.
453
454 **Fig. 4 | The key role of *Neurod1* and *Rfx2* regulator in mouse brain development. a**,
455 Enriched marker TFs for each cluster. **b**, Ranked TFs based on the deviation score and top
456 TFs were listed. **c**, Heatmap showing chromatin accessibility and gene expression of 11772
457 significantly peak-gene linkages. Shown are side-by-side heatmaps in which one row repre-
458 sents a pair of one peak and one linked gene. Each peak can be linked to multiple genes, and
459 each gene can be linked to multiple peaks. the peaks that correlation >=0.7 in peak-gene
460 linkages contained motif of *Neurod1* and *Rfx2* were labeled at right. **d**, Tn5 bias-adjusted tran-
461 scription factor footprints for *Neurod1* motifs. **e-g**, UMAP embedding and spatial mapping of
462 gene scores (e), gene expression (f), TF deviation score and in situ hybridization results (g)
463 from Allen Mouse Brain Atlas at different stages of mouse brain for *Neurod1*. **h-j**, The genome
464 tracks showing the chromatin accessibility (top), peaks site, peaks coaccessibility (middle),
465 peak-gene linkages, gene tracks (bottom), gene expression (right) for *Neurod2* (h), *Neurod6*
466 (i) and *Igfnpl1* (j) in each cluster. *Neurod1* and *Rfx2* motif were shown as gray box.
467
468 **Fig. 5 | Molecular dynamic and gene regularly network of corticogenesis. a**, UMAP show-
469 ing the trajectory of corticogenesis. **b**, Spatial mapping of the trajectory of corticogenesis. **c**,
470 distribution of pseudotime value across development stages. **d**, Scatterplot showing pseudo-
471 time value versus distances to the inner layer of cortex, colored by development stages. **e**.
472 The number of significant correlation peaks for each gene (FDR < 0.01 and PCC > 0.1). Some
473 top TF genes are highlighted. **f**, GO enrichment of top 200 highly enhancer-regulated genes.
474 **g**, Heatmap showing domains of enhancer regulatory (DER), gene expression and residual

along pseudotime. The residual for each gene was calculated by subtracting min-max normalized gene expression from min-max normalized accessibility activity scores. **h**, GO enrichment of each module gene, top 5 significant GO terms for each module are shown (FDR < 0.01). **l**, Scatterplot of Thra motif enrichment among linked peaks versus correlation between gene expression and accessibility activity score. Highlighted are candidate TF regulators of *Thra* with an absolute regulation score > 1. **j**, Accessibility activity score, and gene expression of *Neurod6*, *Thra*, and *Mef2c* in the pseudotime axis. **k**, Gene regulatory network visualization. Edges are colored by signed regulation score. **l**, Schematic of regulatory relationship among *Neurod6*, *Thra*, and *Mef2c* in the corticogenesis trajectory.

Extended Data Fig. 1 | MISAR-seq: workflow, design and library distribution. a, MISAR-seq workflow. The tissue section was first subjected to Tn5 fragmentation, followed by reverse transcription (RT) and finally two rounds of barcode (50 kinds each) ligation on chip. R1, Read1 adaptor. R2, Read2 adaptor. **b**, The composition of microfluidic devices used in this article, including PDMS slab, barcode inlets, acrylic clamp and suction device. **c**, AutoCAD design of PDMS chip with 50μm channel width. **d**, Verification of leakage or diffusion by Cy3 and Fam dye. **e-g**, Size distributions of ATAC library (e), cDNA amplicons (f) and cDNA library (g).

Extended Data Fig. 2 | Data quality of spatial ATAC in MISAR-seq. a, Comparison of percentage of mitochondrial, TSS fragments and FRiP value between MISAR-seq and 10x scATAC-seq, S1, Section1. S2, Section2. Dashed lines indicate the results from Spatial-ATAC-seq[10]. **b-c**, Comparison of insert fragments size distribution (b) and TSS enrichment profiles (c) between MISAR-seq and 10x scATAC-seq.

Extended Data Fig. 3 | TSS enrichment in MISAR-seq. a-i, Comparison of TSS enrichment scatterplot between 10x scATAC-seq (a) and different stages of mouse brain from MISAR-seq (b-i).

Extended Data Fig. 4 | Comparison of peaks called with MISAR-seq and ENCODE bulk ATAC E15.5 brain data. a-c, Comparison of aggregated forebrain (a), midbrain (b) and hindbrain regions (c) of peak-centered heatmap from MISAR-seq and bulk corresponding brain region from ENCODE bulk ATAC E15.5 brain data. **d-f**, The overlap of peaks called from aggregated forebrain (d), midbrain (e) and hindbrain regions (f) of Venn diagram from MISAR-seq and ENCODE datasets. **g**, Quantitative analysis of peaks upset plot called from aggregated forebrain, midbrain and hindbrain regions from MISAR-seq and ENCODE datasets.

Extended Data Fig. 5 | Data quality of spatial RNA in MISAR-seq. a, Comparison of percentage of mitochondrial and ribosome protein per grid between MISAR-seq and DBiT-seq. **b**, Comparison of UMIs and genes number per gird between whether or not add 4% formaldehyde after Tn5 fragmentation in MISAR-seq workflow.

Extended Data Fig. 6 | Spatial chromatin accessibility, gene expression and combined mapping for mouse brain development at E11.0, E13.5, E15.5 and E18.5 from section2. a-c, Spatial ATAC (a), RNA (b) and combined (c) UMAP visualization of different mouse brain development stage, colored by different clusters. **d**, Combined spatial ATAC and RNA UMAP visualization of integrated different mouse brain development stage, colored by different sample sections. **e-g**, Unsupervised clustering of mouse brain sections for spatial ATAC (e), RNA (f) and combined (g).

Extended Data Fig. 7 | Comparison of spatial expression of selected genes with in situ hybridization data from Allen Mouse Brain Atlas. a-f, Spatial mapping of gene expression (RNA) and gene score (ATAC) for selected marker genes, and in situ hybridization of corresponding genes at E11.0, E13.5, E15.5 and E18.5 mouse brain.

Extended Data Fig. 8 | Marker genes analysis for each cluster. a, Peak annotation and proportion plot for each cluster. **b**, Heatmap of spatial ATAC marker peaks across all clusters.

Extended Data Fig. 9 | The genome tracks of representative target genes. a-e, The genome tracks showing the chromatin accessibility (top), peaks site, peaks coaccessibility (middle), peak-gene linkages, gene tracks (bottom), gene expression (right) for *Pou2f2* (a), *Nyap1* (b), *Atp1a3* (c), *Dpysl5* (d) and *Dync1i1* (e) in each cluster. *Neurod1* and *Rfx2* motif were shown as gray box.

Extended Data Fig. 10 | The UMAP embedding and spatial mapping of gene scores, gene expression and deviation scores for represented gene. a, UMAP embedding and spatial mapping of gene scores, gene expression, TF deviation score and in situ hybridization results from Allen Mouse Brain Atlas at different stages of mouse brain for *Rfx2*. **b**, Tn5 bias-adjusted transcription factor footprints for *Neurod1* motifs. **c-e**, UMAP embedding and spatial mapping of gene scores and gene expression for *Igfbpl1* (c), *Neurod2* (d) and *Dync1i1* (e).

Extended Data Fig. 11 | The UMAP embedding and spatial mapping of gene scores, gene expression and deviation scores for represented gene. a, UMAP embedding and spatial mapping of gene scores, gene expression, TF deviation score and in situ hybridization results

547 from Allen Mouse Brain Atlas at different stages of mouse brain for *Pou2f2*. **b-d**, UMAP em-
548 bedding and spatial mapping of gene scores and gene expression for *Nyap1* (b), *Dpysl5* (d)
549 and *Atp1a3* (d).
550
551 **Extended Data Fig. 12 | Putative activators and repressors in cortical development and**
552 **in situ hybridization images of *Thra* and *Mef2c*. a**, TFs ranked by mean regulation score,
553 highlighting top20 putative TF activators (right) versus TF repressors (left). **b-c**, In situ hybrid-
554 ization and expression images of *Thra* (b) and *Mef2c* (c) downloaded from Allen Mouse Brain
555 Atlas.
556
557 **Table S1. DNA oligos used for PCR and preparation of sequencing library.**
558 **Table S2. DNA barcode sequence.**
559 **Table S3. Stat of the MISAR-seq data.**
560
561
562 **Methods**
563
564 **Mice**
565 Mice were maintained in an animal facility approved by the Association for Assessment and
566 Accreditation of Laboratory Animal Care (AAALAC), Guangzhou Institutes of Biomedicine and
567 Health, Chinese Academy of Sciences. Procedures were approved by the Institutional Animal
568 Care and Use Committees of GIBH (Institutional Animal Welfare Assurance Numbers
569 N2019056). Normal brains were collected from wild-type mice of C57BL/6 mice at embryonic
570 days 13.5-18.5. Mice of both sexes were used for the experiments.
571
572 **Mice brain cryosection**
573 Mouse brains at different embryonic stages were dissected, washed with 1x PBS, embedded
574 in OCT (Leica Microsystems), and stored at -80°C for tissue sectioning. Pre-cool the cryostat
575 in advance, set the temperature to -20°C, and set the cutting thickness to 10 μm. Frozen blocks
576 of OCT compounds were removed from cryo-embedding cassettes, and mouse brains from
577 embryos at different stages were cut in sagittal planes, trimmed as needed, and attached to
578 the metal stage of the OCT for cryosectioning. A piece of tissue is attached to each glass slice
579 (188105, CITOTEST Scientific) and stored at -80°C.
580
581 **H&E Staining**

582 The adjacent frozen slide was warmed at room temperature for 10 min and fixed with 200 μL
583 4% formaldehyde for 10 min. After decanting the formaldehyde, 200 μL isopropanol was added
584 to the slide and incubate for 2 min. After completely dried, the tissue section was stained with
585 200 μL hematoxylin (sigma) for 4 min and cleaned in distilled water. The section was then
586 incubated in 200 μL bluing reagent (sigma) for 1 min and rinsed in distilled water. At last, the
587 section was stained with 200 μL eosin (sigma) for 3 min and cleaned in distilled water.
588
589 **Fabrication and assembly of microfluidic device**
590 The device of microfluidic were fabricated using photo lithography. The thickness of the re-
591 sistant and the channel width was 50 μm. The protocol of SU-8 photo lithography, development,
592 and the hard baking was followed based on the manufacturer's (MicroChem) recommenda-
593 tions. The fabricated molds of SU-8 were used to reprint microfluidic resin masters. Last, for
594 microfluidic chips fabrication, polydimethylsiloxane (PDMS) was prepared by mixing base and
595 curing agent at a 10:1 ratio and then poured to the resin masters. After degassing, the PDMS
596 was cured (80°C, 2 h). PDMS slab was cut out after solidification and the inlet and outlet holes
597 were punched for further use.
598
599 **Transposome preparation**
600 Unmodified Tn5 was purchased from manufacturer Vazyme (S601-01), and the
601 transposome was assembled following manufacturer's guidelines. The oligos used for trans-
602 posome assembly were as follows:
603 Tn5 Blocked_ME: /5Phos/C*T*G* T*C*T* C*T*T* A*T*A* C*A*/3ddC/
604 Tn5 Read 1: TCGTCGGCAGCGTCAGATGTGTATAAGAGACAG
605 Tn5 Pho_Read2: /5Phos/GTCTCGTGGGCTCGGAGATGTGTATAAGAGACAG
606 To evaluated the activity of the homemade Tn5, length distribution assay was performed using
607 Qsep100 Bioanalyzer (Bioptic).
608
609 **Preparing oligonucleotides for ligations**
610 There were two rounds of barcode chip ligation in MISAR-seq, each round using a different 50
611 barcodes (Table S2). Hybridization oligos have a universal linker sequence that is partially
612 complementary to specific barcode sequences. These strands anneal before organizing bar-
613 codes to generate DNA molecules with three distinct functional domains: 5' overhangs com-
614 plementary to 5' overhangs on cDNA molecules or transposition DNA molecules (may be de-
615 rived from RT primers, transposition adapters, or a previous round of barcodes), a unique
616 tissue-specific barcode sequence and another 5' overhang that is complementary to the over-
617 hang on the DNA molecule to be ligated. To make 50 different round1 barcode mix in 96-well

618 plate: add 25 μL 100 μM round 1 linker and 25 μL 50 different 100 μM barcodes to 50 different
619 well and anneal the oligonucleotides by heating the plate to 95°C for 2 minutes and cooling to
620 20°C at a rate of about 1°C per minute. All oligonucleotides were dissolved in RNase-free
621 water. The 50 different round2 barcode mix was prepared in the same way.
622
623 **Fixation and blocking**
624 Sagittal sections of mouse brains at different embryonic stages, freshly cut or cryopreserved,
625 were equilibrated at room temperature for 10 min. The tissue was fixed with 1% formaldehyde
626 (252549-500ML, Sigma) for 5 minutes and quenched with 125 mM glycine for 5 min at room
627 temperature. After fixation, the tissue section was quickly dipped in 1X PBS. Then, 1% BSA
628 containing 0.25% RNase inhibitor was added to the tissue slide for blocking at room tempera-
629 ture for 30 min. The tissue was then ready for transposition.
630
631 **Transposition**
632 The tissue section was permeabilized by Omni-ATAC buffer (10 mM Tris-HCl, pH 7.4; 10 mM
633 NaCl; 3 mM MgCl2; 0.1%Tween-20 (P9416-50ML, Sigma); 0.1%NP-40 (11332473001,
634 Roche); 0.01% Digitonin (D141-500MG, Sigma); 1%PIC (05892970001, Roche)) plus 0.25%
635 RNase inhibitor for 10 minutes at room temperature, then was washed with ATAC-RSB buffer
636 (10 mM Tris-HCl pH 7.4; 10 mM NaCl; 3 mM MgCl2; 0.1% Tween-20; 0.25% RNase inhibitor)
637 at room temperature for 5 min. And then the tissue section was washed by RNase free water
638 for three times and air dried. 50 μL transposition buffer containing 0.25% RNase inhibitor (25
639 μL 2X TD buffer (20% Dimethylformamide; 20 mM Tris-HCl pH 7.4; 10 mM MgCl2); 19.4 μL
640 1X DPBS; 0.5 μL 10% Tween-20; 0.1 μL 5% Digitonin; 5 μL transposome) was added followed
641 by incubation at 37°C for 30 minutes. To stop tagmentation, 100 μL TS buffer (20 mM EDTA;
642 1 mM Spermidine) containing 0.25% RNase inhibitor were added after removing transposition
643 buffer. The tissue slide was washed with ATAC-RSB buffer for 1 minute. And then the liquid
644 was removed, the tissue slide was fixed with 4% formaldehyde at room temperature for 20 min
645 and washed with ATAC-RSB buffer and 0.5x PBS.
646
647 **Reverse transcription**
648 Place tissue sections in a humidified box, and each tissue section was mixed with 45 μL of RT
649 mix (final concentration of 1x HiScript III buffer, 0.33 M/μL RNase Inhibitor, 0.5x PBS, 20 M/μL
650 HiScript III Reverse Transcriptase (R302, Vazyme), 500 μM dNTP (18427088, Thermo) and
651 3.5 μM RT primer with an affinity tag). The RT primer contains a poly-T tail, a Unique Molecular
652 Identifier (UMI), a universal ligation overhang, and a biotin molecule. The RT reaction was
653 done with regular procedure.

654 **Ligation**

655 200 μL of ATAC-RSB buffer containing 0.25% RNase inhibitor were added to the tissue area.
656 The slide was gently washed by 200 μL of 1x NEBuffer 3.1. For the first round of ligation,
657 longitudinal PDMS chips were attached in the area of interest and PDMS device were then
658 clamped with an acrylic clamp. The brightfield image was taken with 4x objective (OLYMPUS
659 microscope) for further alignment. 3 μL of Round1 barcode mix (1x T4 DNA ligase buffer, 16
660 M/μL T4 DNA ligase (M0202L, NEB), 0.25 M/μL RNase Inhibitor, NF-H2O, 1x NEBuffer 3.1, 5
661 μM Cy3/Fam dye, 50 μM round1 barcode mix) was added to each inlet well of the chip. The
662 fluid was pulled over slowly with a syringe and the reaction was carried out at 37°C, 80 rpm
663 for 30 min in a wet box. After the reaction, the Cy3 and Fam images were taken by fluores-
664 cence photography. After discarded the ligation solution, the clamp and PDMS chip were re-
665 moved and the tissue slide was washed by RNase free water. 200 μL of ATAC-RSB buffer
666 was added to the tissue area. The second round of barcode ligation was similar to the first
667 round.

668

669 **Tissue digestion**

670 50 μL 2x Lysis buffer (20 mM Tris, pH8.0; 400 mM NaCl; 100 mM EDTA, pH8.0; 4.4%SDS;
671 NF-H2O) and 10 μL proteinase K (20 mg/mL) (RT403-02, TIANGEN) was added to the slide
672 and incubated for 10 min at room temperature. The lysate was further digested at 55 °C 2 h
673 and collected into a 1.5 mL EP tube.

674

675 **cDNA library preparation**

676 RNA sequencing library was generated following the SHARE-seq protocol as previously re-
677 ported with slight modifications. Briefly, the qPCR reaction was carried out at the following
678 conditions: 95°C for 3 min, and then 30 thermal cycles at 98°C for 20 s, 67°C for 20 s and
679 72°C for 3 min. The PCR products were purified by 0.7X Ampure XP beads (A63882, BECK-
680 MAN COULTER) and dissolved in 15 μL RNase free water. cDNA concentration and fragment
681 size distribution were determined by Qsep100 (Bioptic).

682

683 **MISAR-seq RNA library preparation**

684 The cDNA library construction was performed according to the manufacturer's guidelines of
685 TruePrep DNA Library Prep Kit V2 for Illumina (TD502, Vazyme).

686

687 **MISAR-seq ATAC library preparation**

688 Zymo DNA Clean & Concentrator-5 (D4014, ZYMO research) was used to extract the genomic
689 DNA in the supernatant retained after C1 beads purification, and eluted with 25 μL of NF-H2O.

690 20 μL of the eluted purified product was then mixed with the PCR solution (2.5 μL 10 μM
691 Ad1.01~Ad1.08 primer; 2.5 μL 10 μM P7 primer; 25 μL 2x NEBNext Master Mix (M0541, NEB)).
692 Then, PCR was conducted with following the program: 58°C for 5 min, 72 °C for 5 min, 98 °C
693 for 30 s, and then cycled 5 times at 98 °C for 10 s, 65°C for 10 s, and 72°C for 1 min. To
694 determine additional cycles, 5 μL of the pre-amplified mixture was first mixed with the qPCR
695 solution (0.5 μL10 μM Ad1.01~Ad1.08 primer; 0.5 μL 10 μM P7 primer; 1 μL 20x SYBR Green
696 (31000, BIOTIUM); 10 μL 2x NEBNext Master Mix; 2 μL NF-H2O). Then, qPCR reaction was
697 carried out at the following conditions: 98°C for 30 s, and then 30 cycles at 98°C for 10 s, 65°C
698 for 10 s, and 72°C for 1 min. Finally, the remainder 45 μL of the pre-amplified DNA was ampli-
699 fied by running the required number of additional cycles of PCR (cycles needed to reach 1/3
700 of saturated signal in qPCR). The PCR products were further purified by 1X Ampure XP beads
701 and dissolved in 15 μL RNase free water.
702
703 **Sequencing strategy**
704 Both libraries were sequenced on an MGI-seq 2000 sequencer (BGI company) using a pair-
705 end mode. cDNA library was sequenced with read1 75 bp, read2 10 bp, index5 8 bp and
706 index7 50 bp. ATAC library was sequenced with read1 75 bp, read2 75 bp, index5 8 bp and
707 index7 50 bp.
708
709 **MISAR-seq data preprocessing**
710 The sequences were transformed to Cell Ranger ARC format using a custom python script
711 which modified from spatial-ATAC-seq. Resulting fastq files were aligned to mouse genome
712 (mm10) and counted using Cell Ranger ARC v2.0.1. The fragment file and feature barcode
713 matrix file were generated for downstream analysis. To filter the data in non-tissue regions,
714 microscope fluoresce images with two channels were used to identify the pixel locations with
715 manual selection using Adobe Photoshop and generated a mask picture which tissue region
716 was filled with white color while non-tissue region was filled with black color. Then we can use
717 a custom python script to get the filtered barcode location and used to filter fragment file and
718 feature barcode matrix file. The filtered fragments file was then read into ArchR as a tile matrix
719 in 5kb genome binning size using createArrowFiles and ArchRProject function. The filtered
720 feature barcode matrix file was also read into the same ArchR project using import10xFea-
721 tureMatrix and addGeneExpressionMatrix function. Besides, the barcode spatial position ma-
722 trix was read into the same ArchR project using addCellColData function. Both ATAC and RNA
723 data normalization and dimensionality reduction was performed using Latent Semantic Index-
724 ing (LSI) and batch effects was removed by addHarmony function. Besides, the combined of
725 ATAC and RNA reduced dimensions was generated from addCombinedDims function using

726 ATAC and RNA batch removed reduced dimensions. Then, all graph clustering (addClusters
727 function) and Uniform Manifold Approximation and Projection (UMAP) embeddings (addUMAP
728 function) using the batch removed reduced dimensions with default parameters. Gene Score
729 matrix was generated using Gene Score model. Cluster marker genes were calculated using
730 the getMarkerFeatures and getMarkers function (testMethod = "wilcoxon", cutOff = "FDR <=
731 0.05 & log2FC >= 1"). Using the MACS2 to call peaks and motif enrichment or deviations were
732 calculated using peakAnnoEnrichment and addDeviationsMatrix function. Using the cluster-
733 Profiler package to perform GO enrichment analysis (qvalueCutoff = 0.05). To visualize data,
734 the clusters or variable genes were projected into 2D space by UMAP using plotEmbedding
735 function. Spatial clusters were plotted to adjacent H&E-stained tissue by custom R script based
736 on ggplo2 according to the relationship of barcode and location (round1 barcode as column
737 and round2 barcode as row). All functions used in above are from ArchR package.
738
739 **Genes and umi comparison**
740 To equitably compare the number of genes and umis with or without 4% refix before reverse
741 transcription, we use preseq software to exact the same 10M distinct reads for all of the four
742 samples and then performed the barcode split and gene count analysis as MISAR-seq data
743 preprocessing described.
744
745 **The integration of single cell RNA-seq data and MISAR-seq data**
746 We retrieved scRNA data from the developing mouse brain[2]. We downloaded the loom file
747 from Mouse Brain Atlas (http://mousebrain.org/development/downloads.html), which including
748 all gene expression values and annotated metadata per cell. Then the reference data was
749 converted into a seurat object using the scanpy python package of scanpy and R package of
750 Seurat. The E15.5 brain data was selected and the pseudotissue cell type size < 25 was fil-
751 tered out. Meanwhile, mitochondrial and hemoglobin gene also removed for downstream anal-
752 ysis. For E15.5 brain MISAR-seq data, we first read the feature barcode matrix into seurat use
753 Read10X_h5 function from Seurat. The Seurat RNA and ATAC assay was generated by Cre-
754 ateSeuratObject function from Seurat and CreateChromatinAssay function from Signac. Then,
755 for RNA, the SCT assay generated from RNA assay using SCTransform function in Seurat
756 with do.scale = T. For ATAC, the peaks assay was created from new peaks matrix generated
757 by macs2 using the CallPeaks function in Signac. The gene activities assay was generated by
758 GeneActivity function in Signac. For integration of MISAR-seq RNA data with reference, we
759 first use FindIntegrationAnchors function in Seurat of top 2000 high variable genes to find their
760 anchors and then use IntegrateData function in Seurat to integrate both of them. At last, the

new generated integrated assay was used to perform dimensionality reduction and graph clustering use functions in Seurat. The reference data label of pseudotissue was plot with DimPlot function in Seurat. For integration of MISAR-seq ATAC data with reference, we first use the activity assay to perform FindTransferAnchors function in Seurat to find their anchors and then use TransferData function in Seurat to get a imputed scRNA-seq matrix for each of the ATAC grids. After merge reference data and MISAR-seq ATAC data, the new generated combined object was used to perform dimensionality reduction and graph clustering use functions in Seurat. The reference data label of pseudotissue was plot with DimPlot function in Seurat; https://satijalab.org/seurat/index.html.

The single cell deconvolution of MISAR-seq RNA data

The reference of single cell data and MISAR-seq RNA data is almost the same as used in integration above except for the cell type of subclass. For cell-type deconvolution, we used RCTD to deconvolve cell types within a given grid after filtered out cell type size < 25, mitochondrial and hemoglobin gene. We used create.RCTD and run.RCTD function in spacexr package with the 'multi' mode and a mini-mum of 25 cells for each cell-type identity to deconvolve. Other parameters were used with the default; https://github.com/dmcable/spacexr.

Peak co-accessibility and peak-gene linkages

To calculate the peak co-accessibility, we use addCoAccessibility function and getCoAccessibility function from ArchR with default parameters. To find the significant peak-gene linkages, we use addPeak2GeneLinks function and getPeak2GeneLinks function from ArchR with default parameters excepted useMatrix = "GeneExpressionMatrix". To find the *Neurod1* and *Rfx2* motifs in significant peak gene linkages, we exacted the motif position weight matrix (pwm) from chromVARmotifs package and use matchMotifs function from motifmatchr package to match motifs site in peaks. To plot both co-accessibility and peak-gene linkages in genome track, we use plotBrowserTrack function in ArchR with default parameters excepted useMatrix = "GeneExpressionMatrix".

Define spatiotemporal development trajectory of mouse cortex

To incorporate gene expression and peak accessibility to infer corticogenesis trajectory, we selected two clusters that aligned well with cortex anatomy structure and concatenated two batch-removed harmony embedding matrixes as combined latent space. The cellular distance was calculated based on this combined latent space and then fed into the supervised trajectory inference method implemented in the ArchR package.

797 **Linking ATAC peaks and gene expression in the trajectory axis of mouse cortex**
798 To connect cis-regulatory elements with target gene expression, we computed the rolling mean
799 average of peak accessibility and gene expression across the corticogenesis trajectory axis
800 and calculated the Pearson correlation coefficient based on smooth value. Only peaks within
801 250kb on either side of TSS were considered for each gene, especially excluded promoter
802 regions. We retained peak-gene links with FDR < 0.01 and PCC > 0.1, which resulted in 66805
803 significantly putative enhancer-gene linkages. Inspired by the conception of the domain of re-
804 gion accessibility (DORC), we defined domain of enhancer regulatory (DER) by aggregating
805 all linked peak counts of each target gene in a distance-dependent fashion. A generalized
806 linear model was performed to test each gene and accessibility activity for differential expres-
807 sion as a function of pseudotime, which resulted in 1160 putative enhancer-gene interaction
808 pairs. Those interaction pairs were clustered into 5 modules using hierarchical clustering
809 based on euclidean distance. Enrichment analysis was performed using the ClusterProfier for
810 each gene module. The top 5 significant GO terms for each module were shown (FDR < 0.01).
811
812 **Gene regulatory network analysis**
813 Accessibility activity score and gene expression counts were smoothed using 30 nearest
814 neighbors in combined latent space and then fed together with peak-gene links to FigR func-
815 tion 'runFigRGRN' to construct gene regulatory network. TF ranked by the mean regulation
816 score with function 'rankDrivers'.
817
818 **Data quality comparison with other methods**
819 E15.5 mouse forebrain bulk ATAC-seq data was downloaded from ENCODE and E11.0 whole
820 mouse DBiT-seq data (50 μm resolution) was downloaded from GSE137986. Besides, in situ
821 hybridization and expression images were downloaded from Allen Mouse Brain Atlas.
822
823

Fig. 1

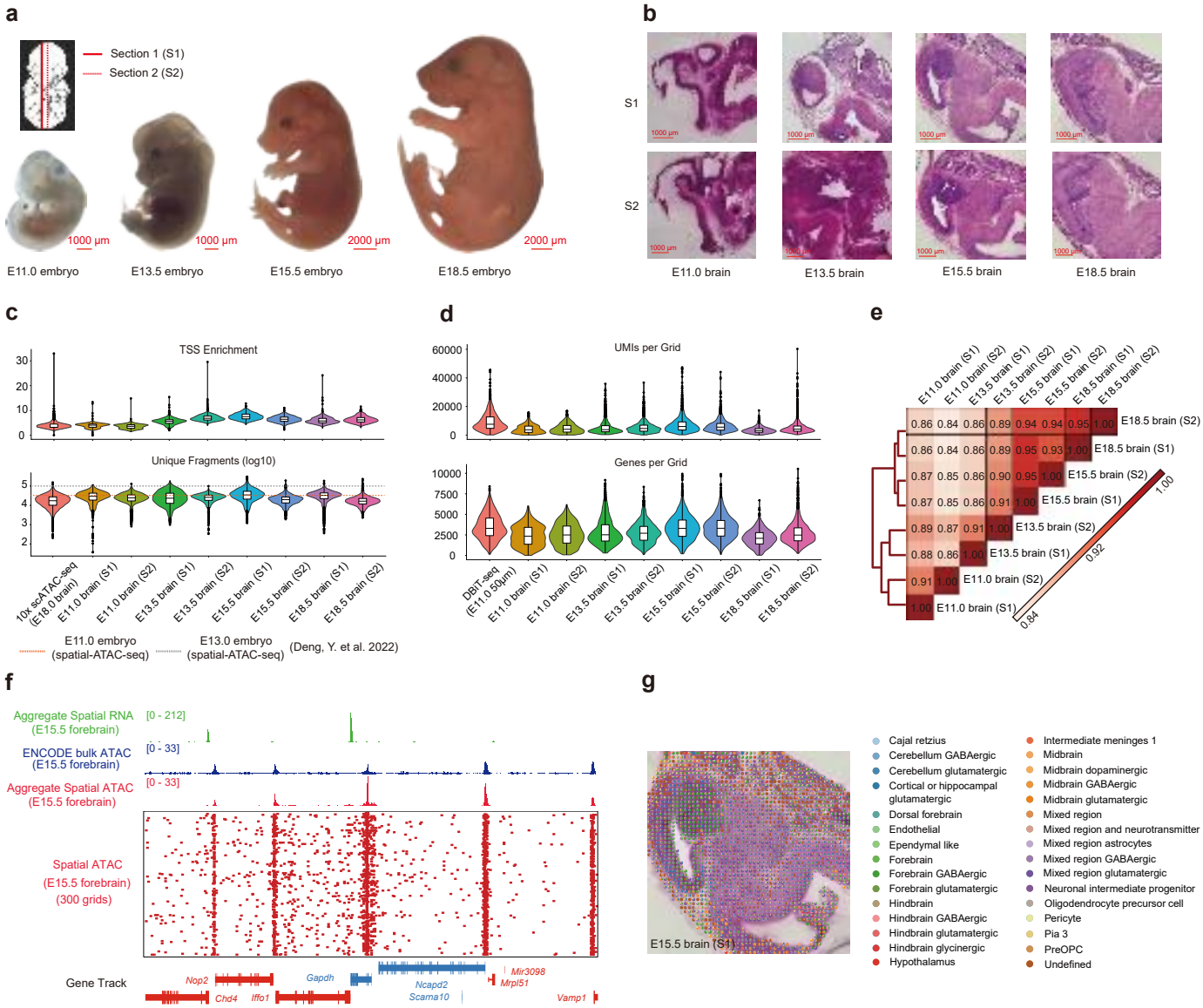
a
Section 1 (S1)
Section 2 (S2)
1000 µm
1000 µm
2000 µm
2000 µm
E11.0 embryo
E13.5 embryo
E15.5 embryo
E18.5 embryo
b
S1
S2
E11.0 brain
E13.5 brain
E15.5 brain
E18.5 brain
c
TSS Enrichment
Unique Fragments (log10)
10x scATAC-seq (E18.0 brain)
E11.0 brain (S1)
E11.0 brain (S2)
E13.5 brain (S1)
E13.5 brain (S2)
E15.5 brain (S1)
E15.5 brain (S2)
E18.5 brain (S1)
E18.5 brain (S2)
E11.0 embryo (spatial-ATAC-seq)
E13.0 embryo (spatial-ATAC-seq)
(Deng, Y. et al. 2022)
d
UMIs per Grid
Genes per Grid
DBiT-seq (E11.0 50µm)
e
E11.0 brain (S1)
E11.0 brain (S2)
E13.5 brain (S1)
E13.5 brain (S2)
E15.5 brain (S1)
E15.5 brain (S2)
E18.5 brain (S1)
E18.5 brain (S2)
f
Aggregate Spatial RNA (E15.5 forebrain)
[0 - 212]
ENCODE bulk ATAC (E15.5 forebrain)
[0 - 33]
Aggregate Spatial ATAC (E15.5 forebrain)
[0 - 33]
Spatial ATAC (E15.5 forebrain) (300 grids)
Gene Track
Nop2
Chd4
Iffo1
Gapdh
Ncapd2
Scarna10
Mir3098
Mrpl51
Vamp1
g
E15.5 brain (S1)
Cajal retzius
Cerebellum GABAergic
Cerebellum glutamatergic
Cortical or hippocampal glutamatergic
Dorsal forebrain
Endothelial
Ependymal like
Forebrain
Forebrain GABAergic
Forebrain glutamatergic
Hindbrain
Hindbrain GABAergic
Hindbrain glutamatergic
Hindbrain glycinergic
Hypothalamus
Intermediate meninges 1
Midbrain
Midbrain dopaminergic
Midbrain GABAergic
Midbrain glutamatergic
Mixed region
Mixed region and neurotransmitter
Mixed region astrocytes
Mixed region GABAergic
Mixed region glutamatergic
Neuronal intermediate progenitor
Oligodendrocyte precursor cell
Pericyte
Pia 3
PreOPC
Undefined
h
ATAC
forebrain dorsal
forebrain ventral
forebrain ventro lateral
hindbrain
midbrain
UMAP2
UMAP1
forebrain dorsal
forebrain ventral
forebrain ventro lateral
midbrain
hindbrain
this study (ATAC)
Reference data
i
ATAC
forebrain dorsal pallium (intermediate)
forebrain dorsal pallium (ventricular)
forebrain dorsal pallium (superficial)
forebrain subpallium
midbrain & hindbrain
hindbrain
cartilage
j
ATAC
E15.5 brain (S1)
k
RNA
hindbrain
forebrain ventral
forebrain dorsal
midbrain
forebrain ventro lateral
forebrain dorsal
forebrain ventral
forebrain ventro lateral
midbrain
hindbrain
this study (RNA)
Reference data
l
RNA
forebrain dorsal pallium (ventricular)
hindbrain
forebrain dorsal pallium (intermediate)
cartilage
forebrain subpallium
midbrain
forebrain dorsal pallium (superficial)
midbrain & hindbrain
m
RNA
E15.5 brain (S1)

Fig. 2

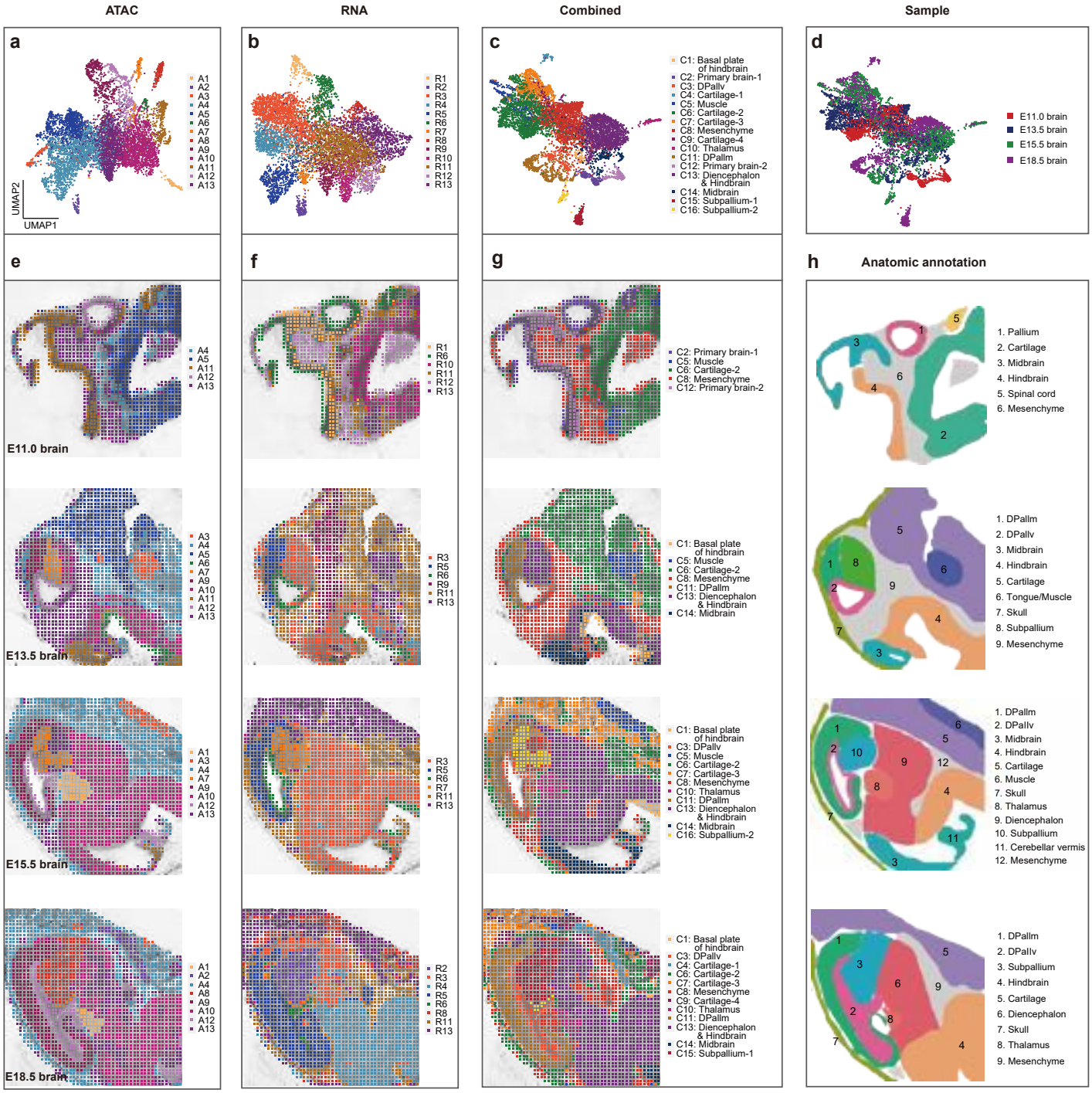
ATAC
RNA
Combined
Sample
a
UMAP2
UMAP1
A1
A2
A3
A4
A5
A6
A7
A8
A9
A10
A11
A12
A13
b
R1
R2
R3
R4
R5
R6
R7
R8
R9
R10
R11
R12
R13
c
C1: Basal plate of hindbrain
C2: Primary brain-1
C3: DPallv
C4: Cartilage-1
C5: Muscle
C6: Cartilage-2
C7: Cartilage-3
C8: Mesenchyme
C9: Cartilage-4
C10: Thalamus
C11: DPallm
C12: Primary brain-2
C13: Diencephalon & Hindbrain
C14: Midbrain
C15: Subpallium-1
C16: Subpallium-2
d
E11.0 brain
E13.5 brain
E15.5 brain
E18.5 brain
e
f
g
h
Anatomic annotation
1. Pallium
2. Cartilage
3. Midbrain
4. Hindbrain
5. Spinal cord
6. Mesenchyme
1. DPallm
2. DPallv
3. Midbrain
4. Hindbrain
5. Cartilage
6. Tongue/Muscle
7. Skull
8. Subpallium
9. Mesenchyme
1. DPallm
2. DPallv
3. Midbrain
4. Hindbrain
5. Cartilage
6. Muscle
7. Skull
8. Thalamus
9. Diencephalon
10. Subpallium
11. Cerebellar vermis
12. Mesenchyme
1. DPallm
2. DPallv
3. Subpallium
4. Hindbrain
5. Cartilage
6. Diencephalon
7. Skull
8. Thalamus
9. Mesenchyme

Fig. 3

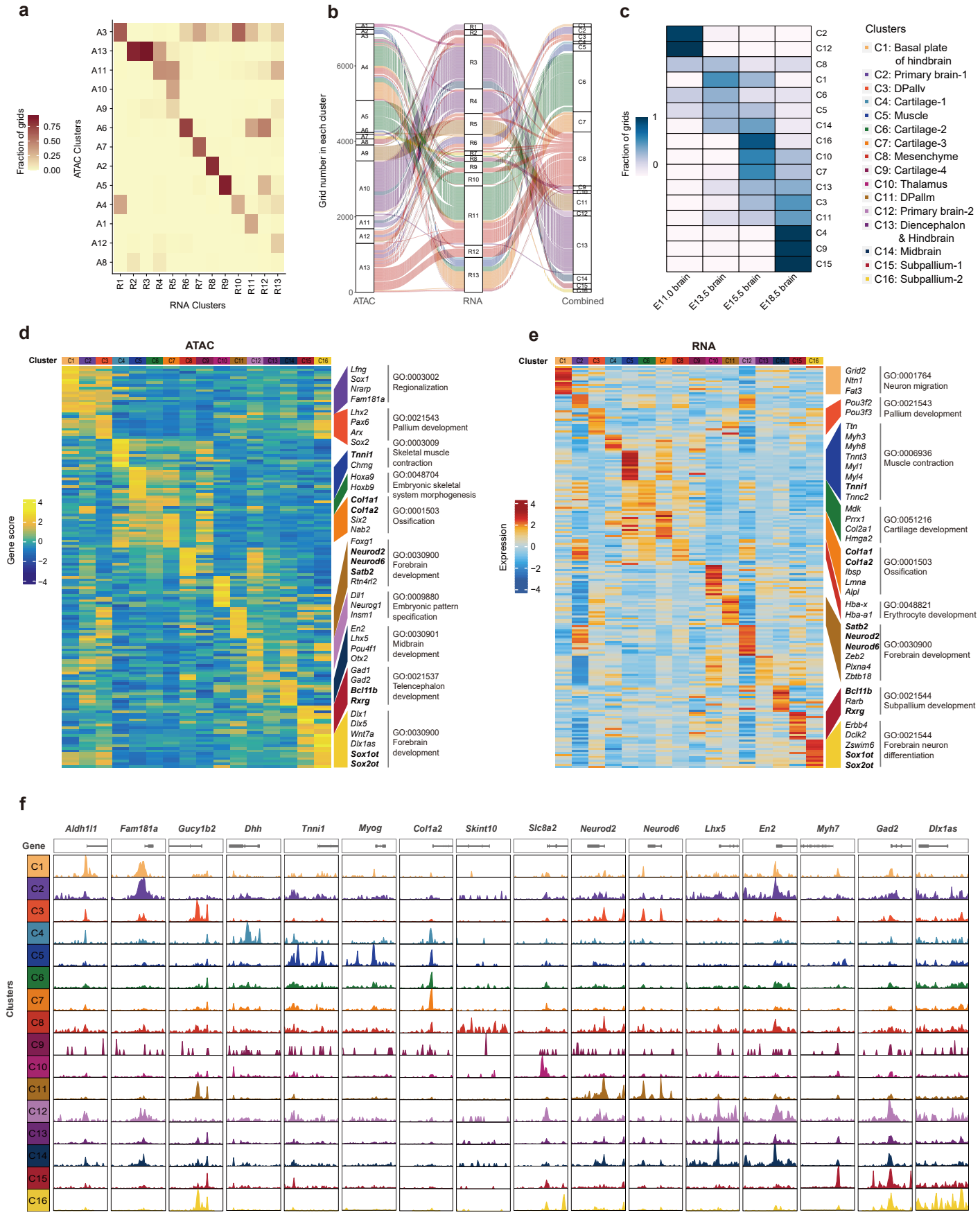
a
Fraction of grids
0.75
0.50
0.25
0.00
ATAC Clusters
A3
A13
A11
A10
A9
A6
A7
A2
A5
A4
A1
A12
A8
R1 R2 R3 R4 R5 R6 R7 R8 R9 R10 R11 R12 R13
RNA Clusters
b
Grid number in each cluster
6000
4000
2000
0
ATAC
RNA
Combined
c
Fraction of grids
1
0
E11.0 brain
E13.5 brain
E15.5 brain
E18.5 brain
Clusters
C1: Basal plate of hindbrain
C2: Primary brain-1
C3: DPallv
C4: Cartilage-1
C5: Muscle
C6: Cartilage-2
C7: Cartilage-3
C8: Mesenchyme
C9: Cartilage-4
C10: Thalamus
C11: DPallm
C12: Primary brain-2
C13: Diencephalon & Hindbrain
C14: Midbrain
C15: Subpallium-1
C16: Subpallium-2
d
ATAC
Cluster
Gene score
4
2
0
−2
−4
Lfng Sox1 Nrarp Fam181a GO:0003002 Regionalization
Lhx2 Pax6 Arx Sox2 GO:0021543 Pallium development
GO:0003009
Tnni1 Chrng Skeletal muscle contraction
Hoxa9 Hoxb9 GO:0048704 Embryonic skeletal system morphogenesis
Col1a1 Col1a2 Six2 Nab2 GO:0001503 Ossification
Foxg1 Neurod2 Neurod6 Satb2 Rtn4rl2 GO:0030900 Forebrain development
Dll1 Neurog1 Insm1 GO:0009880 Embryonic pattern specification
En2 Lhx5 Pou4f1 Otx2 GO:0030901 Midbrain development
Gad1 Gad2 Bcl11b Rxrg GO:0021537 Telencephalon development
Dlx1 Dlx5 Wnt7a Dlx1as Sox1ot Sox2ot GO:0030900 Forebrain development
e
RNA
Cluster
Expression
4
2
0
−2
−4
Grid2 Ntn1 Fat3 GO:0001764 Neuron migration
Pou3f2 Pou3f3 GO:0021543 Pallium development
Ttn Myh3 Myh8 Tnnt3 Myl1 Myl4 Tnni1 Tnnc2 GO:0006936 Muscle contraction
Mdk Prrx1 Col2a1 Hmga2 GO:0051216 Cartilage development
Col1a1 Col1a2 Ibsp Lmna Alpl GO:0001503 Ossification
Hba-x Hba-a1 GO:0048821 Erythrocyte development
Satb2 Neurod2 Neurod6 Zeb2 Plxna4 Zbtb18 GO:0030900 Forebrain development
Bcl11b Rarb Rxrg GO:0021544 Subpallium development
Erbb4 Dclk2 Zswim6 Sox1ot Sox2ot GO:0021544 Forebrain neuron differentiation
f
Aldh1l1 Fam181a Gucy1b2 Dhh Tnni1 Myog Col1a2 Skint10 Slc8a2 Neurod2 Neurod6 Lhx5 En2 Myh7 Gad2 Dlx1as
Gene
Clusters
C1 C2 C3 C4 C5 C6 C7 C8 C9 C10 C11 C12 C13 C14 C15 C16

Fig. 4

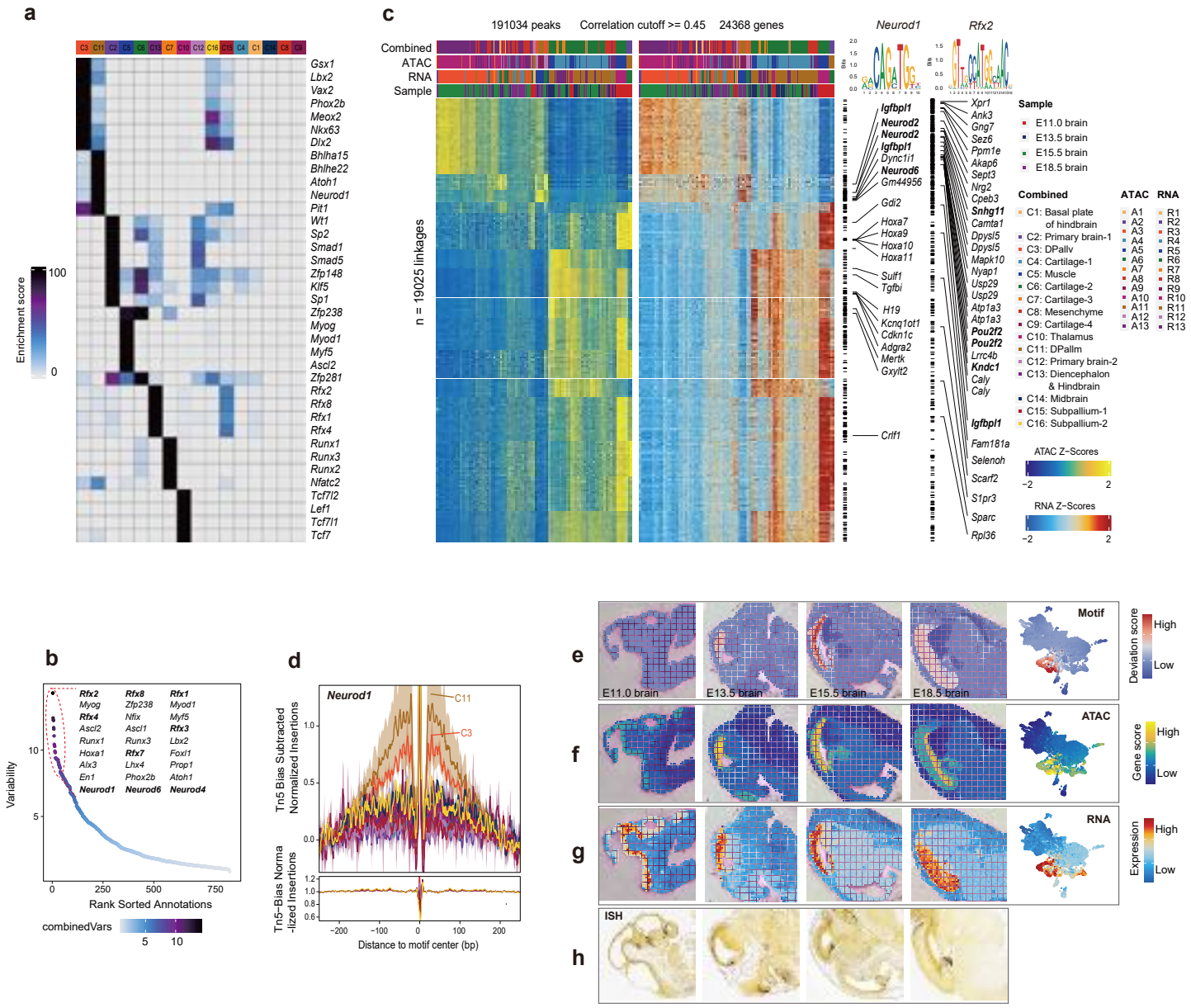
a
Enrichment score
100
0
Gsx1
Lbx2
Vax2
Phox2b
Meox2
Nkx63
Dlx2
Bhlha15
Bhlhe22
Atoh1
Neurod1
Pit1
Wt1
Sp2
Smad1
Smad5
Zfp148
Klf5
Sp1
Zfp238
Myog
Myod1
Myf5
Ascl2
Zfp281
Rfx2
Rfx8
Rfx1
Rfx4
Runx1
Runx3
Runx2
Nfatc2
Tcf7l2
Lef1
Tcf7l1
Tcf7
c
191034 peaks
Correlation cutoff >= 0.45
24368 genes
Combined
ATAC
RNA
Sample
n = 19025 linkages
Neurod1
Rfx2
Sample
E11.0 brain
E13.5 brain
E15.5 brain
E18.5 brain
Combined
C1: Basal plate of hindbrain
C2: Primary brain-1
C3: DPallv
C4: Cartilage-1
C5: Muscle
C6: Cartilage-2
C7: Cartilage-3
C8: Mesenchyme
C9: Cartilage-4
C10: Thalamus
C11: DPallm
C12: Primary brain-2
C13: Diencephalon & Hindbrain
C14: Midbrain
C15: Subpallium-1
C16: Subpallium-2
ATAC
A1 A2 A3 A4 A5 A6 A7 A8 A9 A10 A11 A12 A13
RNA
R1 R2 R3 R4 R5 R6 R7 R8 R9 R10 R11 R12 R13
ATAC Z-Scores
−2
2
RNA Z-Scores
−2
2
b
Variability
Rank Sorted Annotations
combinedVars
5
10
d
Neurod1
C11
C3
Tn5 Bias Subtracted Normalized Insertions
Tn5−Bias Normalized Insertions
Distance to motif center (bp)
e
f
g
h
Motif
ATAC
RNA
ISH
Deviation score
Gene score
Expression
High
Low
i
chr11:98279644−98379645
Neurod1 motif
Expression
Peaks
CoAccessibility
Peak2GeneLinks
Genes
value
j
chr6:55631262−55731263
Neurod1 motif
Expression
k
chr4:45776826−45876827
Neurod1 & Rfx2 motif
Expression

Fig. 5

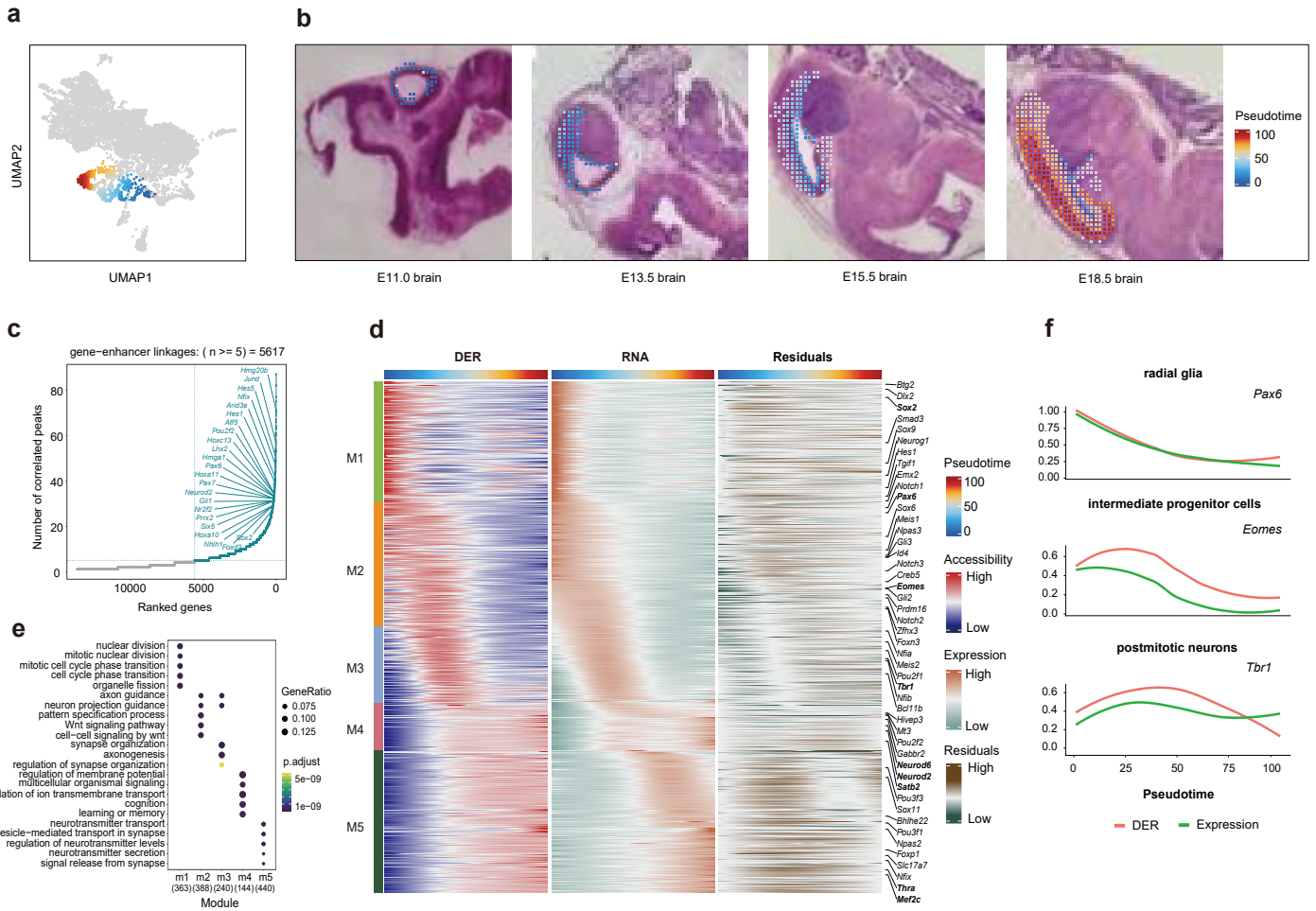
a
UMAP2
UMAP1
b
Pseudotime
100
50
0
E11.0 brain
E13.5 brain
E15.5 brain
E18.5 brain
c
gene−enhancer linkages: (n >= 5) = 5617
Number of correlated peaks
Ranked genes
e
GeneRatio
p.adjust
Module
d
DER
RNA
Residuals
M1
M2
M3
M4
M5
Pseudotime
Accessibility
Expression
Residuals
High
Low
f
radial glia
Pax6
intermediate progenitor cells
Eomes
postmitotic neurons
Tbr1
Pseudotime
DER
Expression

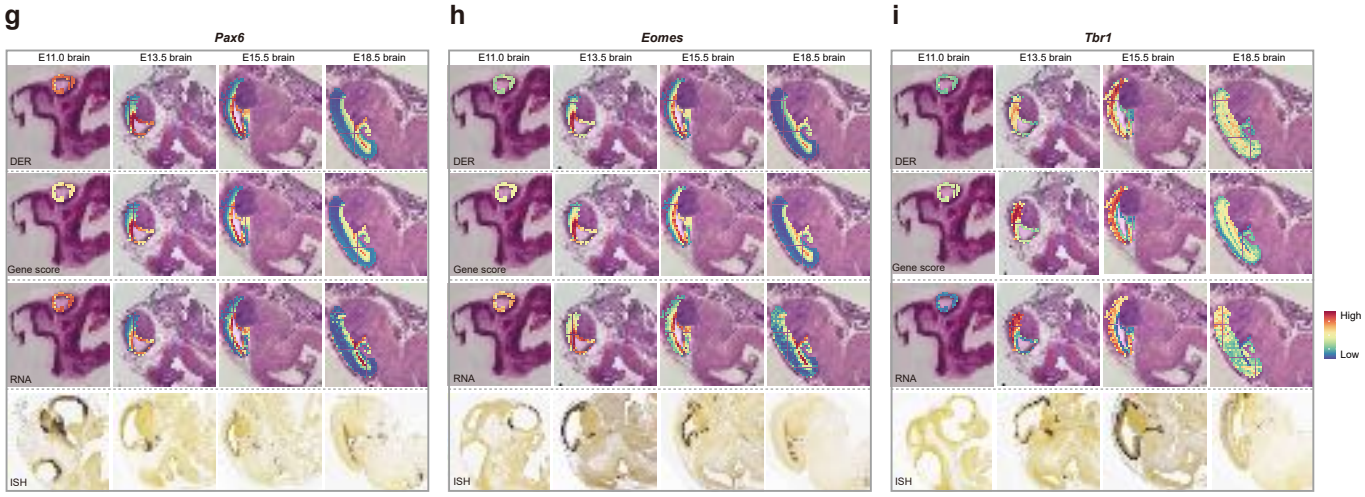
g
Pax6
h
Eomes
i
Tbr1
E11.0 brain
E13.5 brain
E15.5 brain
E18.5 brain
DER
Gene score
RNA
ISH
High
Low

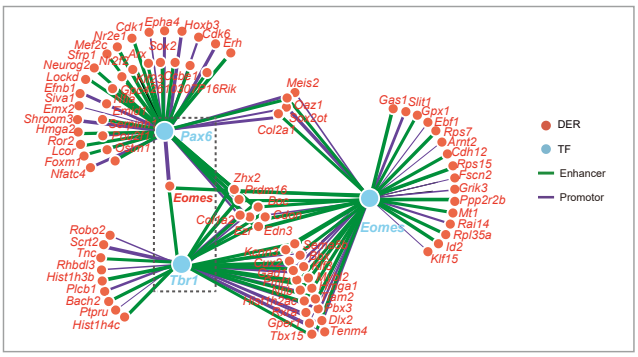
j
Pax6
Eomes
Tbr1
DER
TF
Enhancer
Promotor

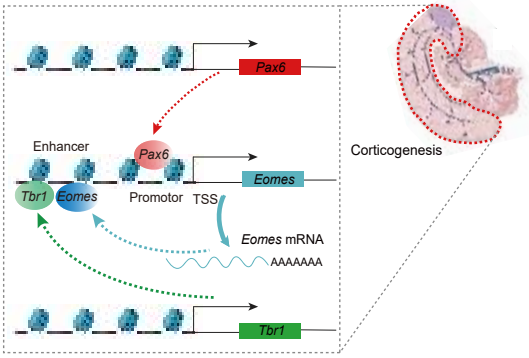
k
Pax6
Enhancer
Pax6
Eomes
Tbr1
Eomes
Promotor
TSS
Eomes mRNA
AAAAAAA
Tbr1
Corticogenesis

Extended Data Fig. 1

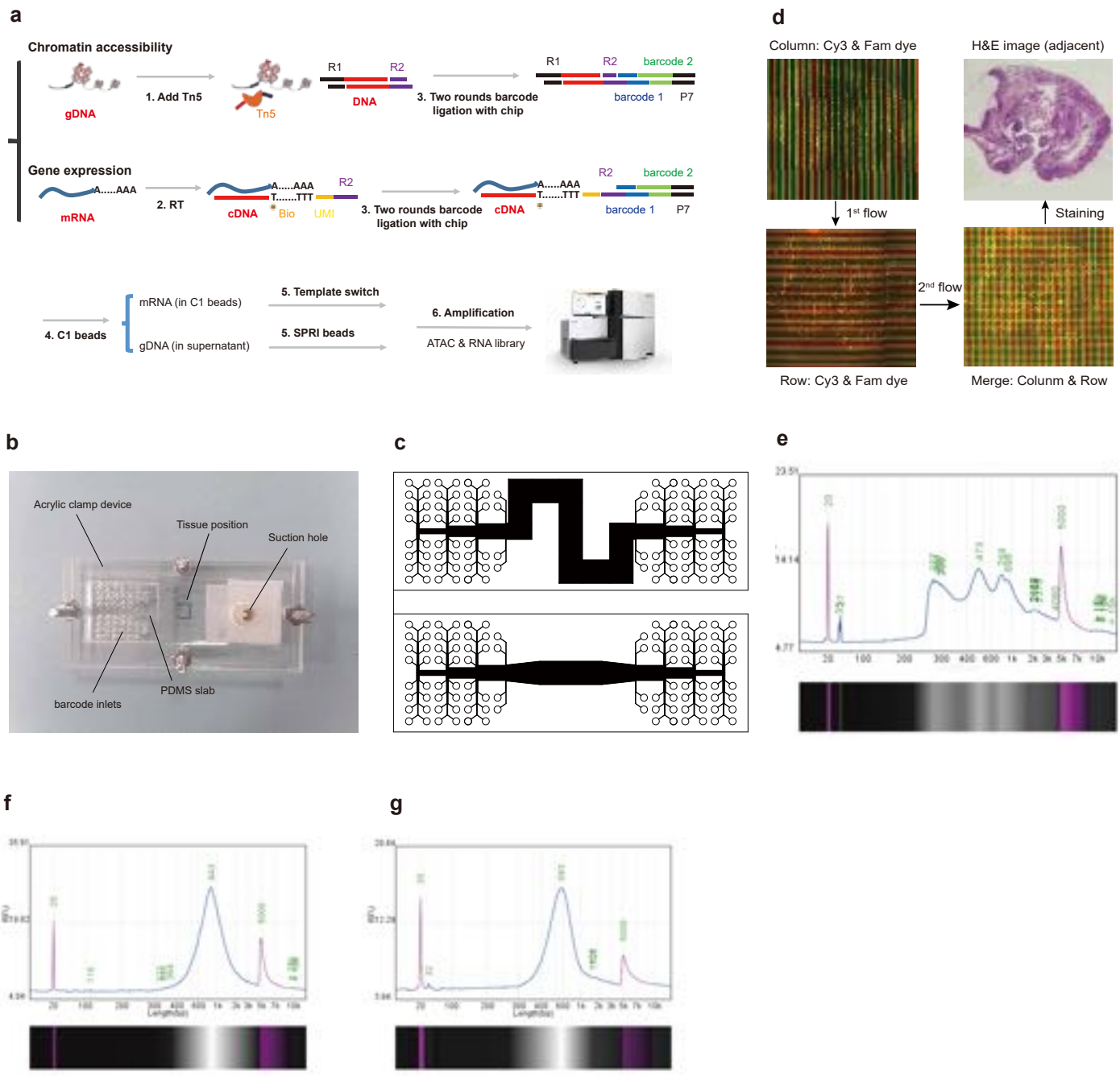

Extended Data Fig. 2

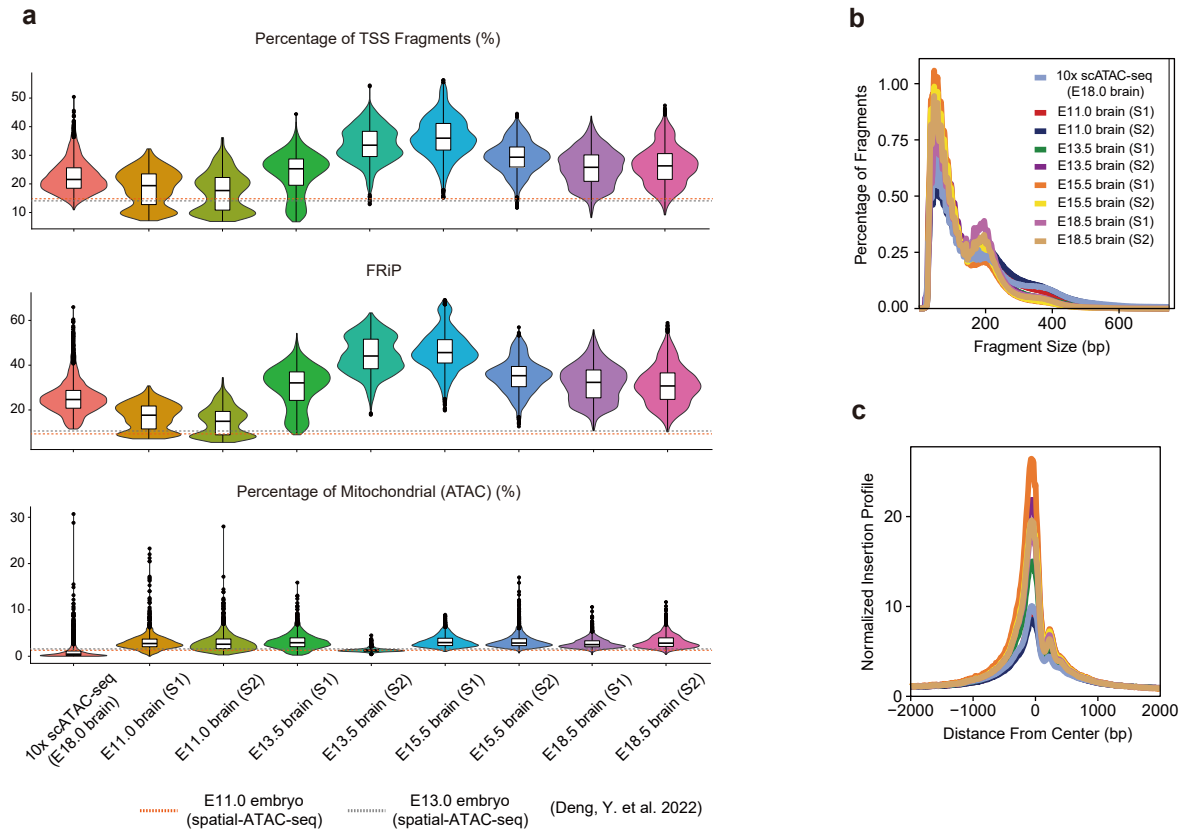

Extended Data Fig. 3

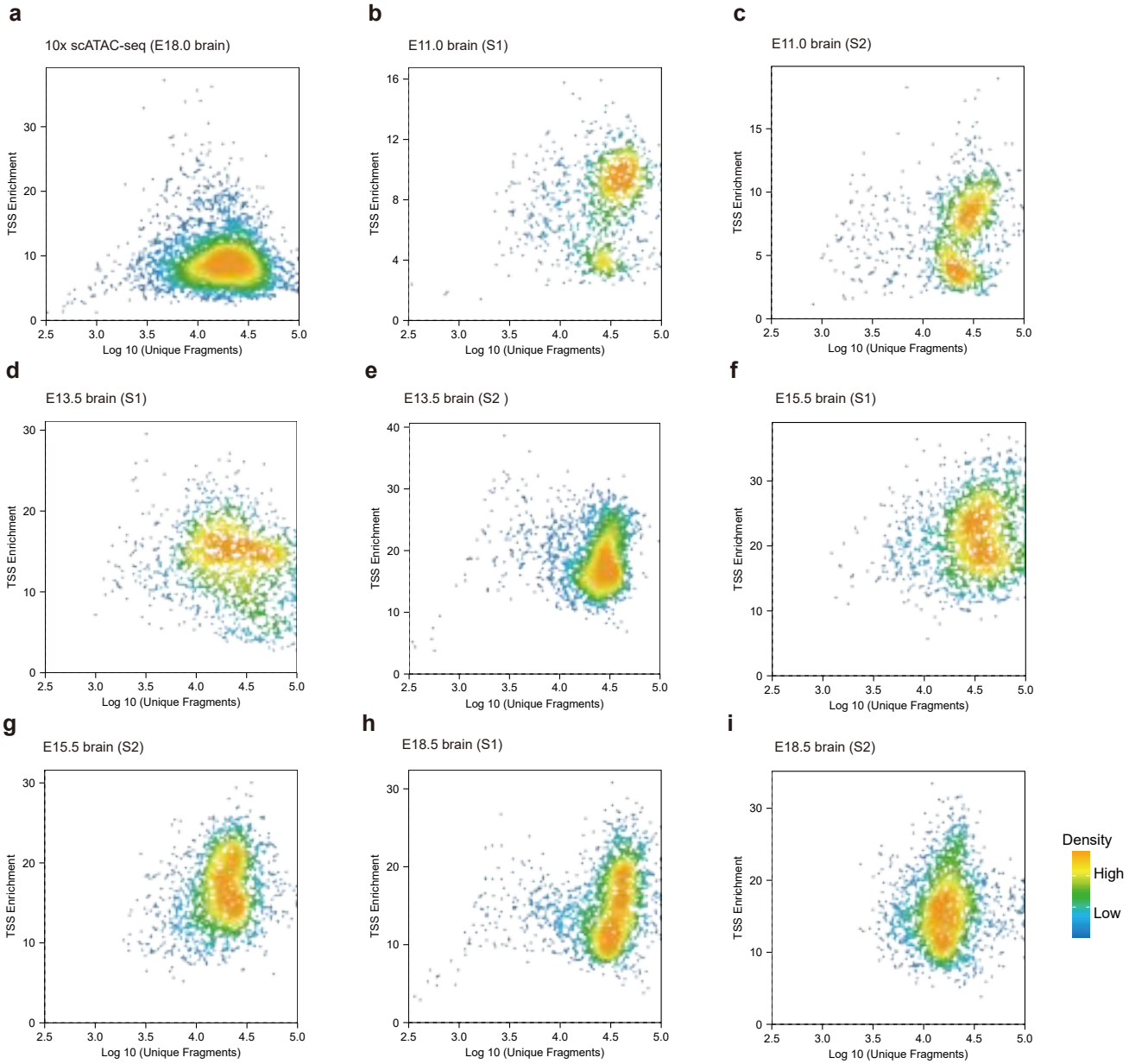

Extended Data Fig. 4

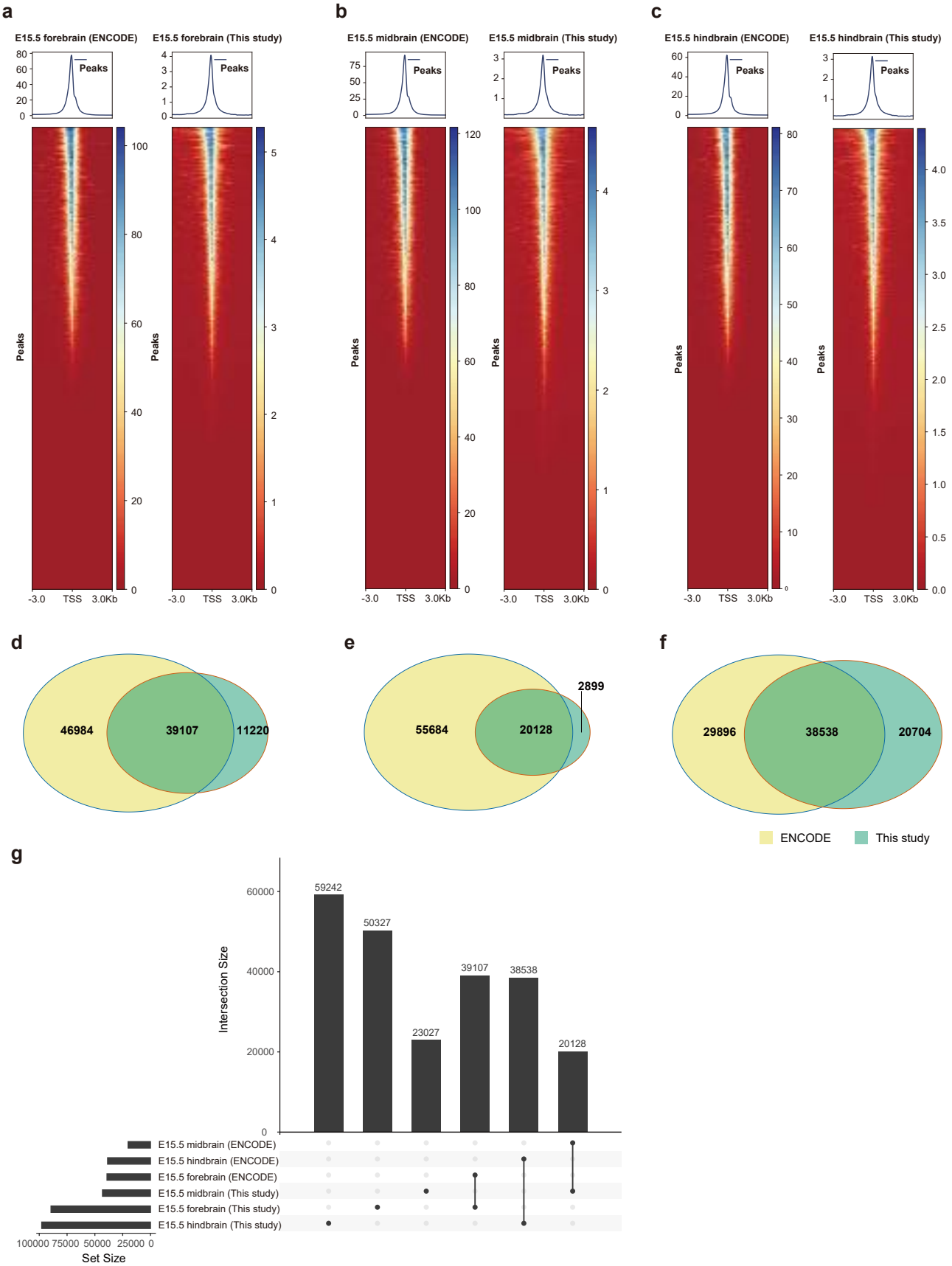

Extended Data Fig. 5

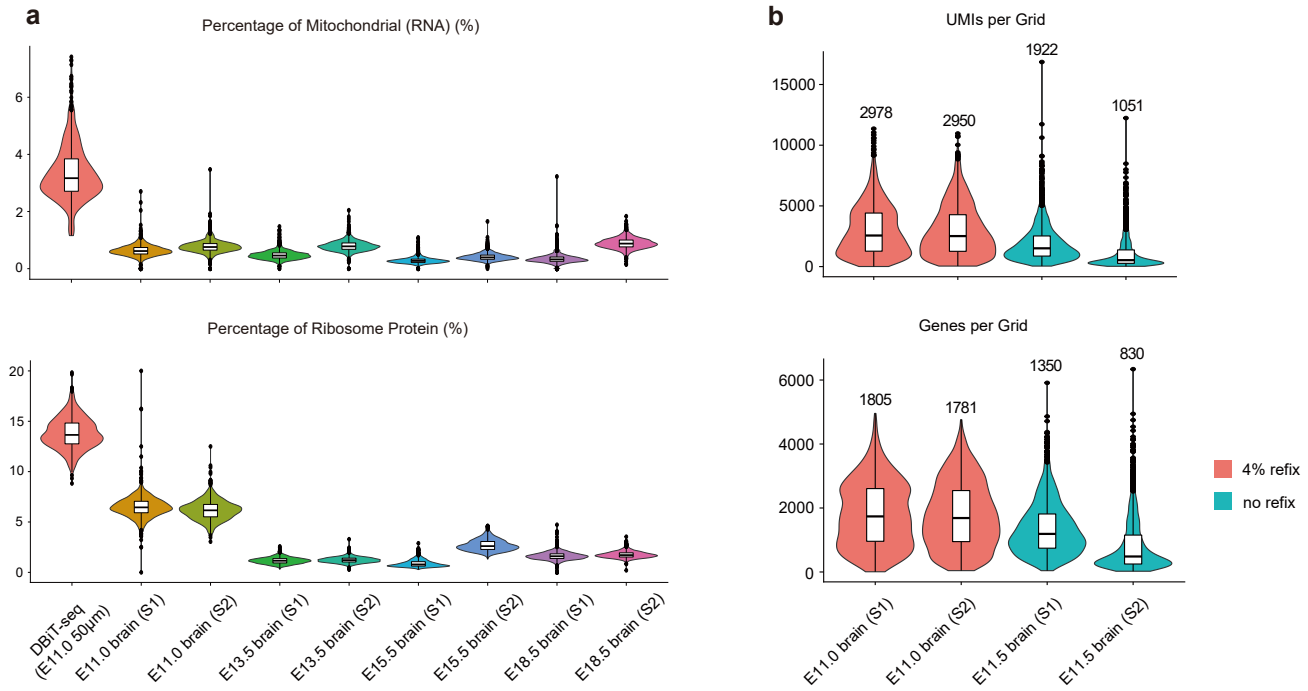

Extended Data Fig. 6

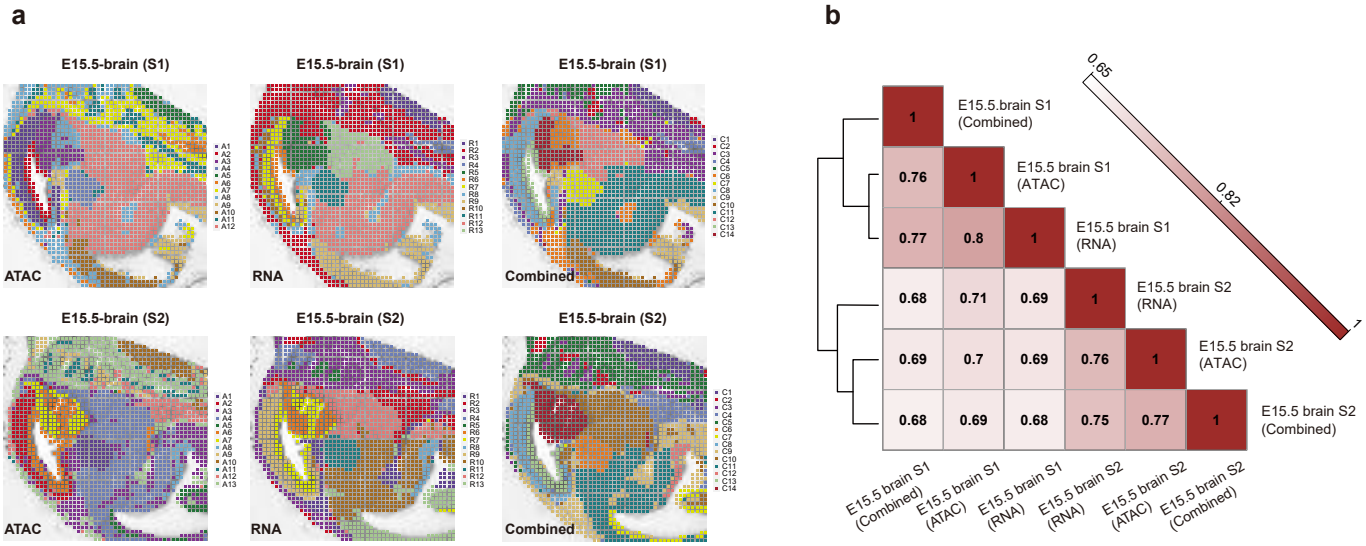

Extended Data Fig. 7

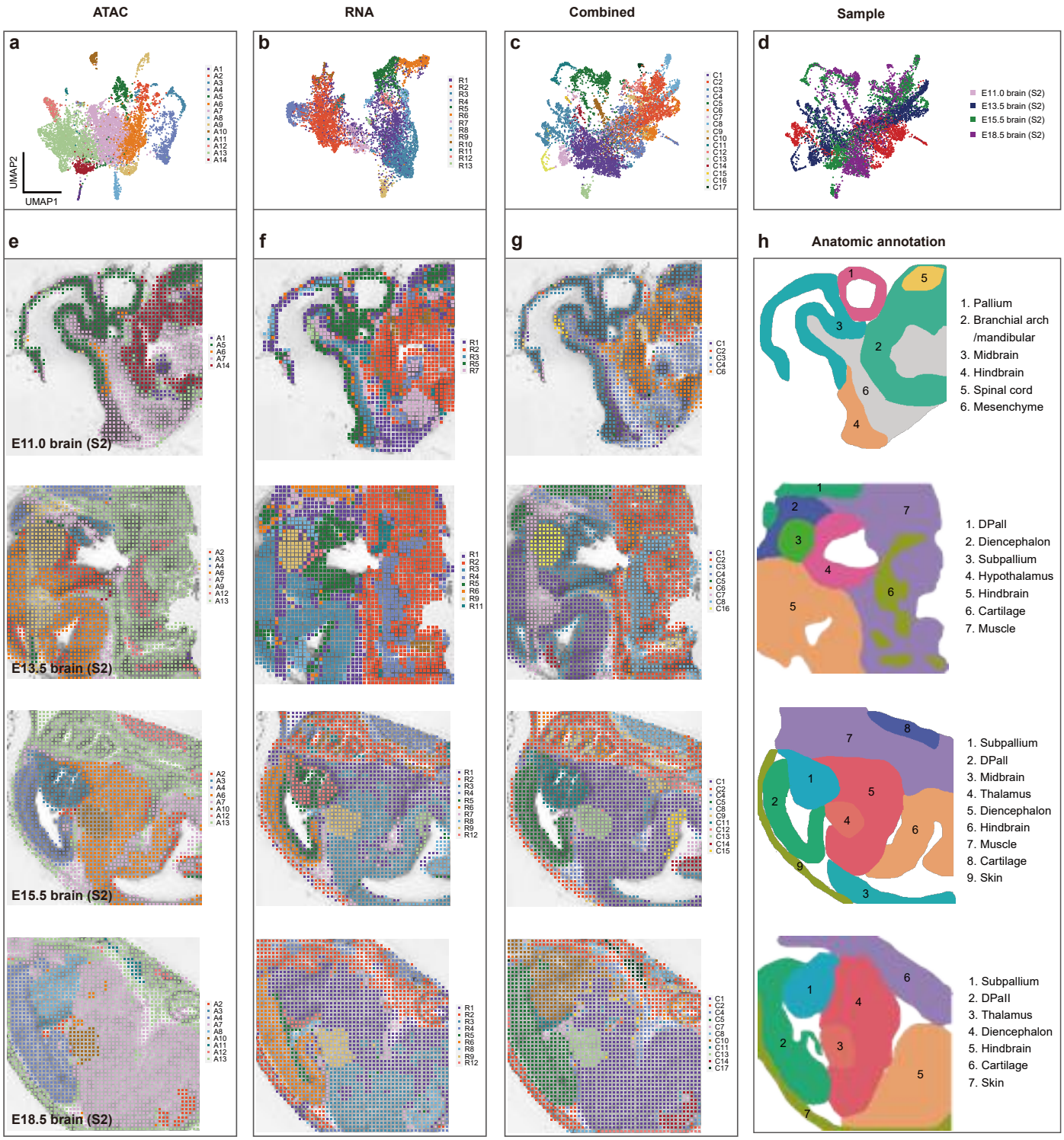

Extended Data Fig. 8

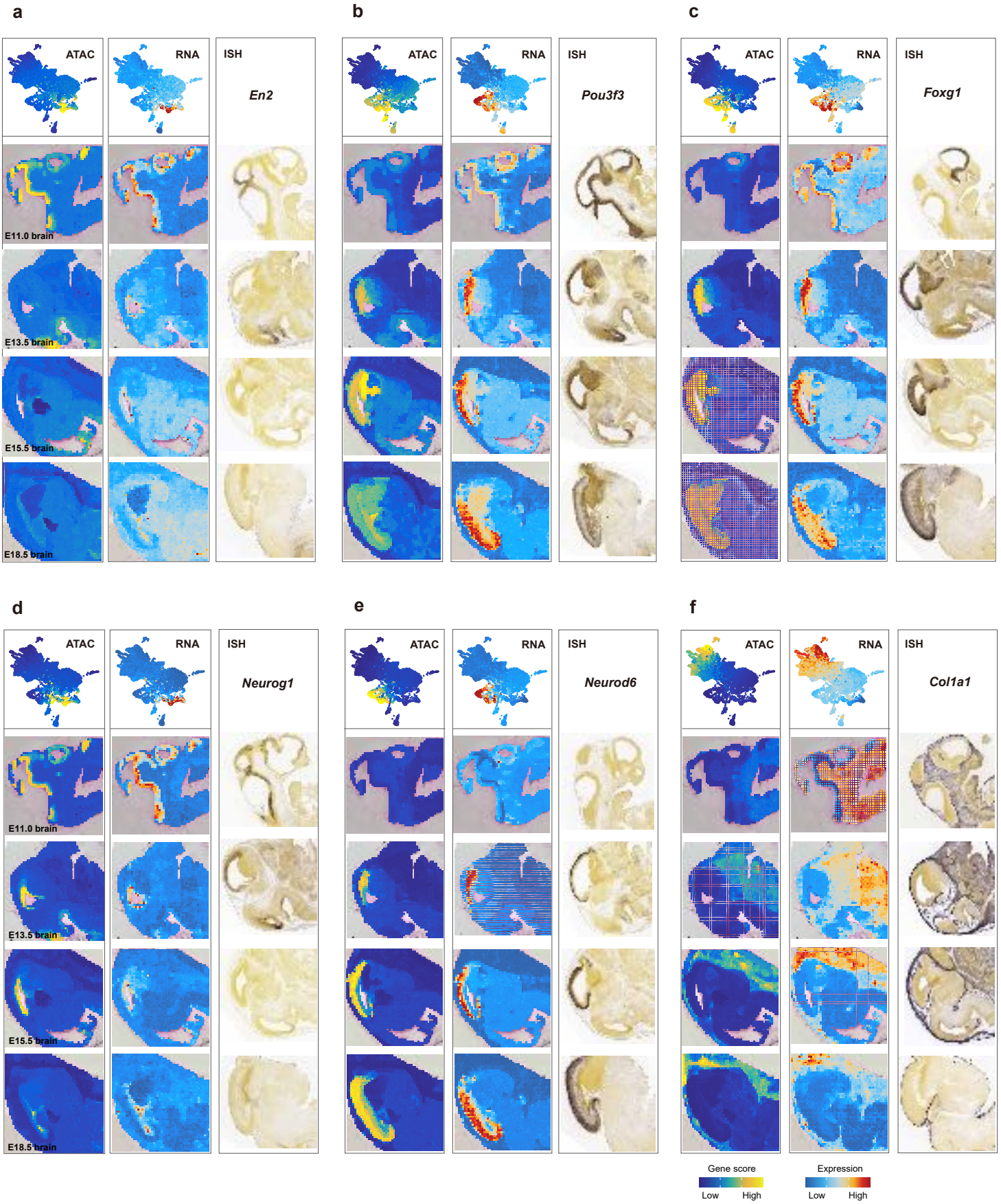

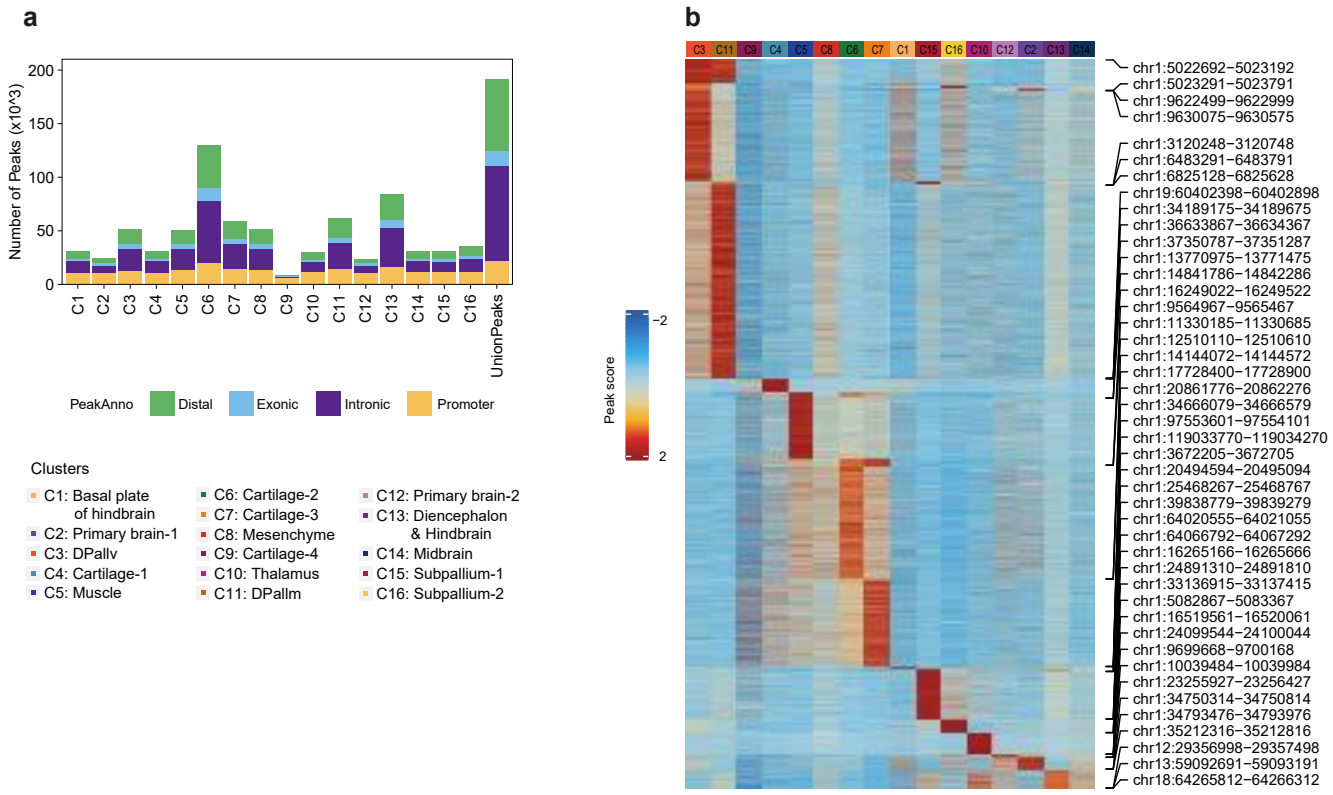
a
Number of Peaks (x10^3)
200
150
100
50
0
C1
C2
C3
C4
C5
C6
C7
C8
C9
C10
C11
C12
C13
C14
C15
C16
UnionPeaks
PeakAnno
Distal
Exonic
Intronic
Promoter
Clusters
C1: Basal plate of hindbrain
C2: Primary brain-1
C3: DPallv
C4: Cartilage-1
C5: Muscle
C6: Cartilage-2
C7: Cartilage-3
C8: Mesenchyme
C9: Cartilage-4
C10: Thalamus
C11: DPallm
C12: Primary brain-2
C13: Diencephalon & Hindbrain
C14: Midbrain
C15: Subpallium-1
C16: Subpallium-2
b
C3 C11 C9 C4 C5 C8 C6 C7 C1 C15 C16 C10 C12 C2 C13 C14
Peak score
−2
2
chr1:5022692−5023192
chr1:5023291−5023791
chr1:9622499−9622999
chr1:9630075−9630575
chr1:3120248−3120748
chr1:6483291−6483791
chr1:6825128−6825628
chr19:60402398−60402898
chr1:34189175−34189675
chr1:36633867−36634367
chr1:37350787−37351287
chr1:13770975−13771475
chr1:14841786−14842286
chr1:16249022−16249522
chr1:9564967−9565467
chr1:11330185−11330685
chr1:12510110−12510610
chr1:14144072−14144572
chr1:17728400−17728900
chr1:20861776−20862276
chr1:34666079−34666579
chr1:97553601−97554101
chr1:119033770−119034270
chr1:3672205−3672705
chr1:20494594−20495094
chr1:25468267−25468767
chr1:39838779−39839279
chr1:64020555−64021055
chr1:64066792−64067292
chr1:16265166−16265666
chr1:24891310−24891810
chr1:33136915−33137415
chr1:5082867−5083367
chr1:16519561−16520061
chr1:24099544−24100044
chr1:9699668−9700168
chr1:10039484−10039984
chr1:23255927−23256427
chr1:34750314−34750814
chr1:34793476−34793976
chr1:35212316−35212816
chr12:29356998−29357498
chr13:59092691−59093191
chr18:64265812−64266312

Extended Data Fig. 10

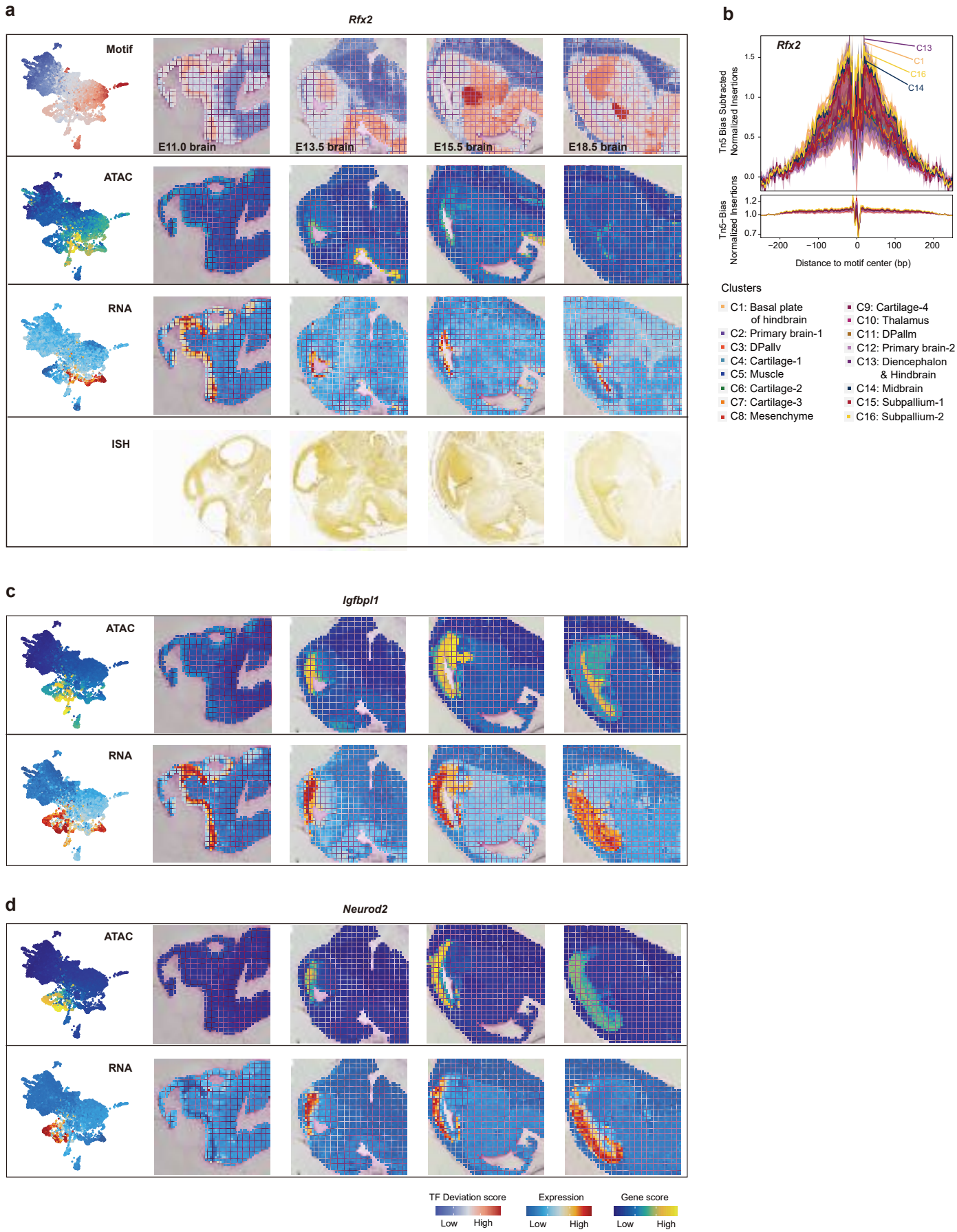

Extended Data Fig. 11

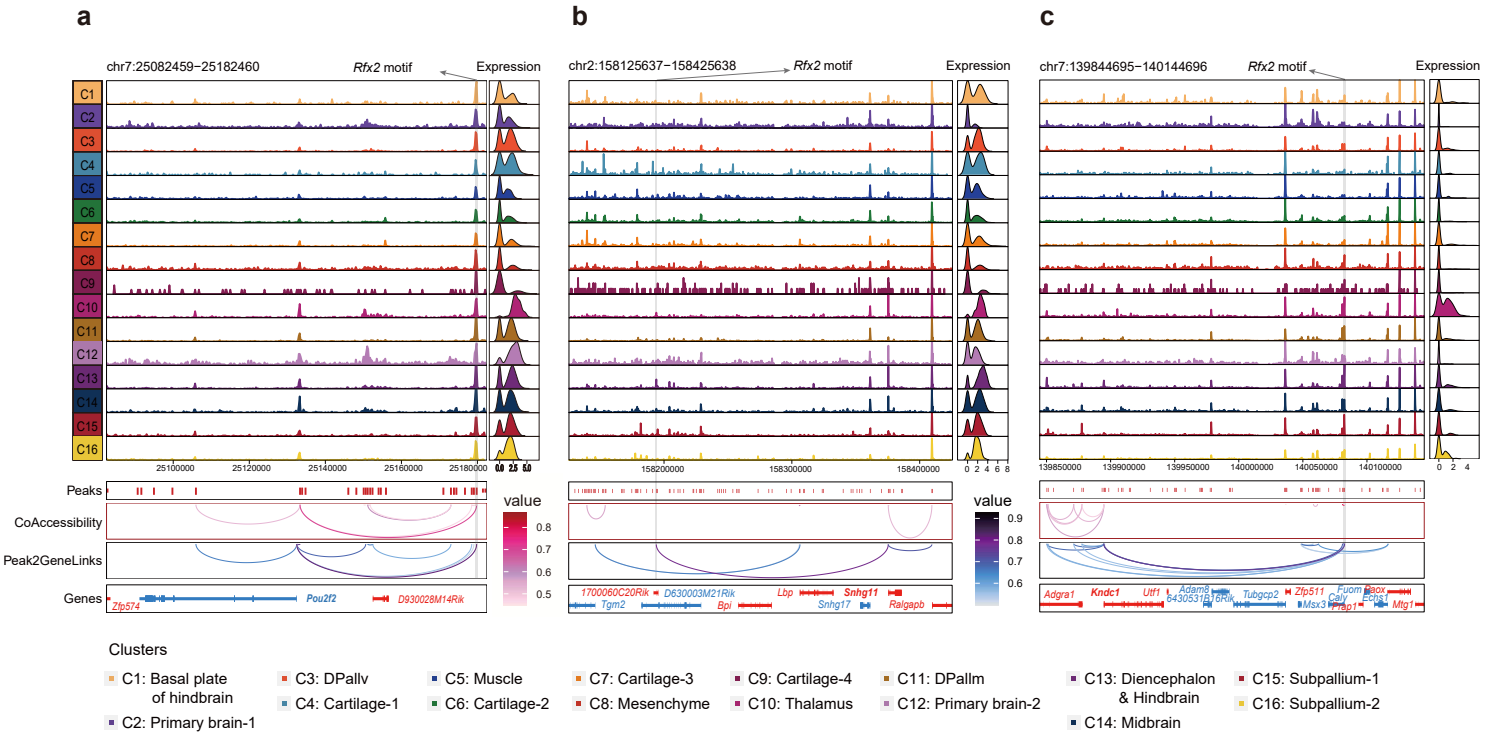

Clusters

- C1: Basal plate of hindbrain
- C2: Primary brain-1
- C3: DPallv
- C4: Cartilage-1
- C5: Muscle
- C6: Cartilage-2
- C7: Cartilage-3
- C8: Mesenchyme
- C9: Cartilage-4
- C10: Thalamus
- C11: DPallm
- C12: Primary brain-2
- C13: Diencephalon & Hindbrain
- C14: Midbrain
- C15: Subpallium-1
- C16: Subpallium-2

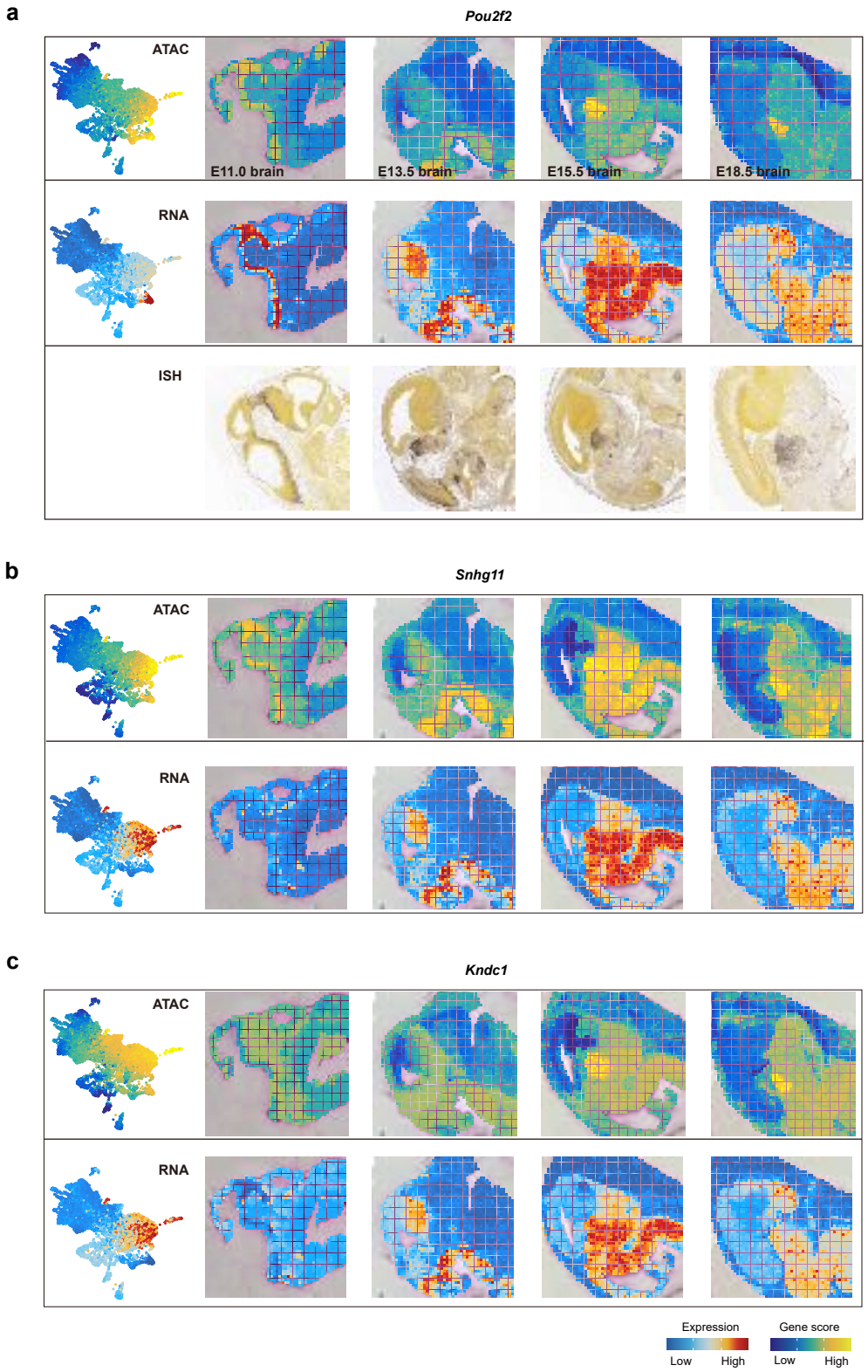
a
Pou2f2
ATAC
RNA
ISH
E11.0 brain
E13.5 brain
E15.5 brain
E18.5 brain
b
Snhg11
ATAC
RNA
c
Kndc1
ATAC
RNA
Expression
Low
High
Gene score
Low
High

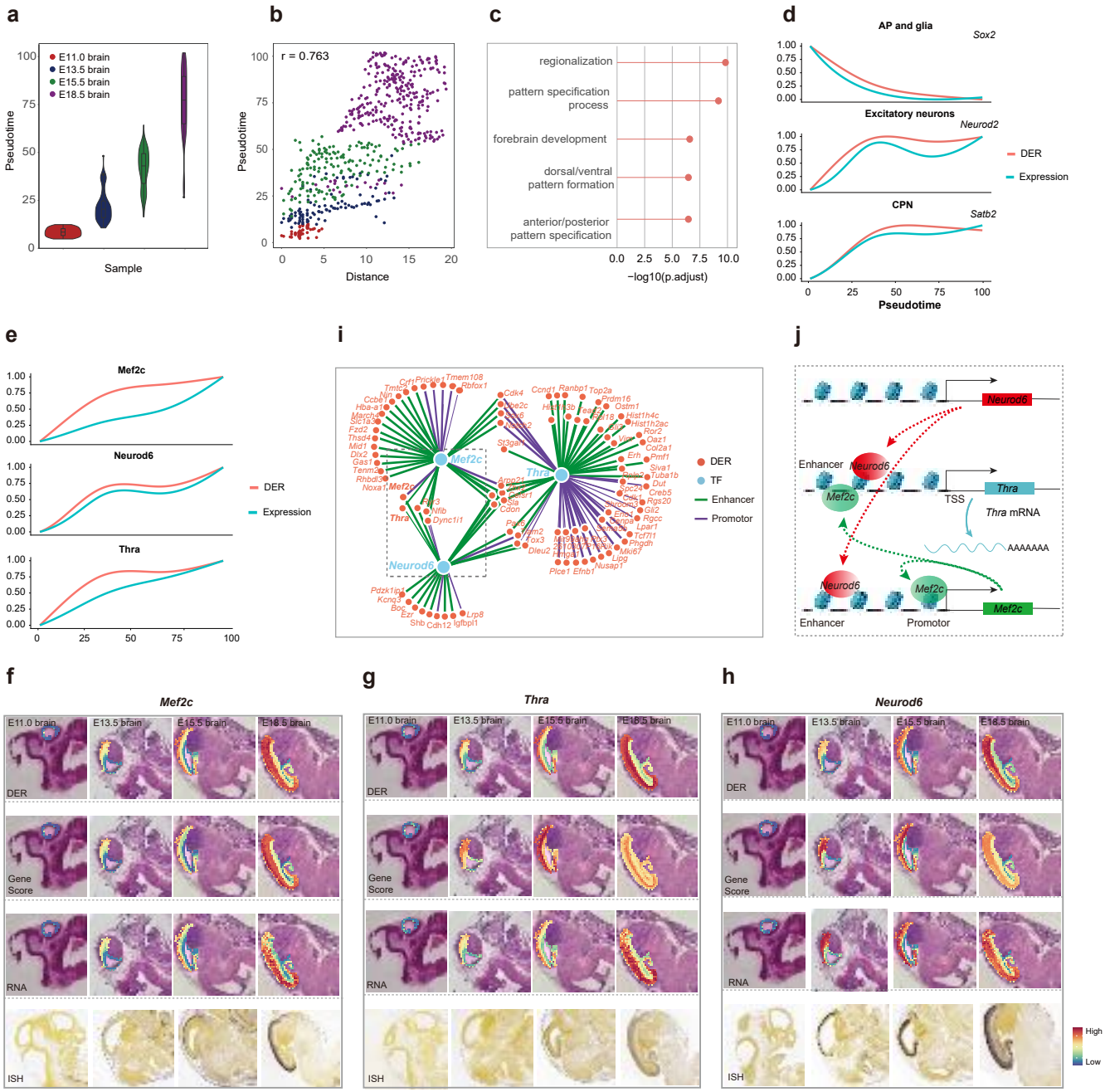
a
E11.0 brain
E13.5 brain
E15.5 brain
E18.5 brain
Pseudotime
Sample
b
r = 0.763
Pseudotime
Distance
c
regionalization
pattern specification process
forebrain development
dorsal/ventral pattern formation
anterior/posterior pattern specification
−log10(p.adjust)
d
AP and glia
Sox2
Excitatory neurons
Neurod2
CPN
Satb2
DER
Expression
Pseudotime
e
Mef2c
Neurod6
Thra
DER
Expression
i
Mef2c
Thra
Neurod6
DER
TF
Enhancer
Promotor
j
Neurod6
Enhancer
Mef2c
Thra
TSS
Thra mRNA
AAAAAAA
Neurod6
Mef2c
Enhancer
Promotor
f
Mef2c
E11.0 brain
E13.5 brain
E15.5 brain
E18.5 brain
DER
Gene Score
RNA
ISH
g
Thra
h
Neurod6
High
Low